An Integrated Localization and Control Framework for Multi-Agent Formation

Yang Cai, *Student Member, IEEE*, and Yuan Shen, *Member, IEEE*

***Abstract*—High-accuracy formation is essential for multi-agent systems to accomplish certain tasks, and the accuracy of the formation is determined jointly by the network localization and formation control procedures. Existing studies commonly treat the two procedures separately in the system design, leading to suboptimal formation performance. This paper establishes a general framework for high-accuracy multi-agent formation via integrated localization and control. In particular, we propose a new metric called the formation error to characterize the minimum squared distance between two formations for arbitrary translation and rotation, and develop an integrated localization and control scheme to minimize the mean formation error (MFE). Theoretical bounds for the MFE are derived in a closed form, which guides the integrated design of the sensing strategy and control policy. In the case study, we develop efficient integrated algorithms for multi-agent formation under spectrum resource constraints. Numerical results validate the performance gain of the proposed algorithms over existing ones as well as demonstrate the effects of the network parameters on formation performance.**

***Index Terms*—Formation control, formation error, integrated localization and control, resource allocation.**

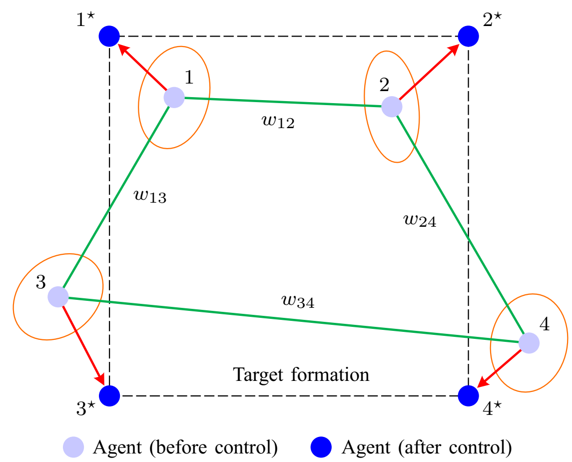

Fig. 1. MAF example: A network of four agents aims to form a target formation (a square). The agents (blue nodes) with position uncertainty (orange area) first make inter-node measurements (green lines) with spectrum resource w_{ij} for link (i, j); and then estimate their formation and collaboratively control their movements to adjust the actual formation to the target formation.

I. Introduction

Multi-agent systems can leverage the cooperation among agents to accomplish complicated missions that one single agent is hardly capable of, in both military and civil sectors. For example, with the development of unmanned autonomous vehicle (UAV) techniques, multiple or even swarms of UAVs can be coordinated to perform dangerous or confidential tasks. The potential applications include target detection and tracking [1], surveillance and reconnaissance [2], stereo reconstruction and mapping [3], Internet of vehicles [4], communication relaying [5], and precision agriculture [6]. In many of these emerging applications, the system performance highly depends on the accuracy of the formation, calling for the advancement of multi-agent formation (MAF) techniques with high accuracy and efficiency [7].

Existing schemes for MAF usually decompose the task into two procedures, namely *network localization* and *formation control* [8]. Specifically, the agents first estimate their positions by position-related measurements in network localization; and then based on the position estimates, the agents collaboratively control their movements to adjust the actual formation to the target formation in formation control. In the two-procedure task, the accuracy of the position estimates from network localization is critical to the performance of the formation control. A common approach for network localization uses the global positioning system (GPS), where the agent positions are estimated by the pseudo-range measurements between the agents and the satellites. However, GPS may not be able to provide sufficient localization accuracy for MAF applications, or even fails in the presence of interference or obstacle shadowing [9]. To this end, inter-node measurements such as the round-trip time (RTT) and the angle of arrival (AoA) can be employed to further improve the localization accuracy by cooperative techniques [10]–[12]. Indeed, the inter-node measurements are particularly helpful for MAF since the relative position information provided by these measurements is directly related to the geometry of the network.

In the field of network localization, theoretical frameworks for cooperative localization based on wideband transmission are established, and the fundamental limits of the localization accuracy are derived under various network settings [13]–[15]. Several localization algorithms, such as the multidimensional scaling (MDS) [16] and the semidefinite programming (SDP) [17], are proposed for practical cooperative localization networks. Specially, localization based on relative measurements between the agents fits within the scope of the MAF. Questions related to self-localizability are studied, and several graph-

Y. Cai was with the Department of Electronic Engineering, Tsinghua University, Beijing 100084, China. He is now with the Department of Electrical Engineering, University of Southern California, Los Angeles, CA 90089-2565 USA (e-mail: yangcai@usc.edu).

Y. Shen is with the Department of Electronic Engineering, Tsinghua University, Beijing 100084, China, and Beijing National Research Center for Information Science and Technology, Beijing 100084, China (e-mail: shenyuan_ee@tsinghua.edu.cn).

theory based algorithms are developed [18]–[20]. To enhance the localization accuracy under resource constraints such as power and spectrum, recent studies were devoted to designing the sensing strategy with resource allocation [21]–[23]. In the context of MAF, it is also desirable to use the resource efficiently in improving the formation performance. However, the sensing strategy designed for network localization is not necessarily suitable for MAF due to two main differences between MAF and network localization, especially relative localization [24]–[26]. First, the given target formation is the basis for evaluating the MAF performance, whereas only the position estimation errors are of concern in network localization. Second, MAF includes a successive procedure of formation control, in addition to network localization. Thus, we need to define a new performance metric for MAF and to design the sensing strategies under a given control policy.

In the robotic community, existing studies on formation control can be divided into graph-based and velocity-based methods [27]–[29], or their combination termed as "flocking with shape control" [30]. Specially, the graph-based methods operate on the geometry of the current network, and the agent positions are adjusted to form the actual formation as the target formation [31]–[33]. The objective of a control policy is mainly towards the stability [34], and the evaluation usually depends on the probability of convergence to the target formation in static networks [35], or the deviation of the agents' actual trajectories from the planned ones in dynamic networks [36]. There are two challenges to apply existing methods to high-accuracy MAF: the existing criteria do not sufficiently characterize the accuracy of MAF, and most existing methods only employ the position estimates, but not fully exploit the statistical information of the measurements. These again require a new performance metric for MAF and motivate us to incorporate the statistical information when designing the control policy.

Recently, much research interest is motivated to design localization and control procedures in an integrated way for MAF. Several algorithms aiming for simultaneous localization and formation control are developed [37]–[39]. In [37], orientation alignment of the agents is tackled in addition to position estimation as well as formation control; in [38], a novel distributed relative localization algorithm is combined with the complex Laplacian based formation control. In this work, we focus on exploiting the advantages of integrating the two procedures from the perspective of information. Some preliminary results validate that adjusting localization strategy according to the control policy can effectively leverage the MAF performance [40]. To realize this goal, the two key questions need to be addressed:

- how to perform network localization that provides the most useful information for MAF;
- how to design formation control that fully exploits the statistical information in the measurements.

In this paper, we investigate the high-accuracy MAF problem in mobile wireless networks, and propose an integrated localization and control (ILC) framework. As a case study, we propose a joint design of sensing strategies and control policies for MAF under spectrum resource constraints. The main contributions of this work are summarized as follows:

- We establish an analytical framework for MAF in the presence of measurement noises and control errors, and propose an ILC scheme for MAF;
- We propose a new metric called the formation error, which characterizes the minimum squared distance between the actual formation and the target formation for arbitrary translation and rotation, and derive the theoretical bounds for the mean formation error (MFE); and
- We formulate an optimization problem to minimize the MFE under resource constraints via joint design of the sensing strategy and the control policy, and develop an efficient algorithm for practical systems.

The rest of this paper is organized as follows. Section II describes the system model, and Section III defines the formation error and reveals some of its properties. Section IV derives the theoretical bounds for the MFE, followed by the optimization formulation for ILC in Section V. Section VI presents several numerical results, and conclusions are drawn in last section.

TABLE I
COMMONLY USED SYMBOLS

Symbol	Description
$\boldsymbol{x}$	Actual formation (collecting the positions of all nodes).
$\boldsymbol{\xi}$	(A realization of) target formation (collecting the positions of all nodes in a network of target geometry).
$\boldsymbol{r}$	The collection of all measurements.
$\boldsymbol{c}$	Aggregated control vector for the entire formation.
$\mathcal{F}(\boldsymbol{q})$	Equivalent formation set of formation $\boldsymbol{q}$.
$\ell(\boldsymbol{x},\boldsymbol{\xi})$	Formation error between two formations $\boldsymbol{x}$ and $\boldsymbol{\xi}$.
$\bar{\ell},\bar{\ell}_{\perp},\bar{\ell}_{/\!/}$	Mean formation error, and its orthogonal and parallel components.
$\boldsymbol{w}$	Resource allocation vector.

Notations: The n-dimensional real number space is denoted by $\mathbb{R}^n$, and vectors are written as bold letters $\boldsymbol{x}$ and matrices as bold capital letters $\boldsymbol{X}$. The random variables and random vectors are written as x and bold letters $\mathbf{x}$, respectively. $[\cdot]^{\mathrm{T}}$, $[\cdot]^{-1}$ and $\mathrm{tr}\{\cdot\}$ denote the transpose, inverse and trace of its argument, respectively. Column vectors of size m with all 0's and 1's are respectively denoted as $\mathbf{0}_m$ and $\mathbf{1}_m$, and $\boldsymbol{I}_m$ and $\boldsymbol{O}_m$ represent the $m\times m$ identity and zero matrices. The directional vector is defined as $\boldsymbol{u}(\theta)=[\cos\theta\ \ \sin\theta]^{\mathrm{T}}$. For two symmetric matrices $\boldsymbol{X}$ and $\boldsymbol{Y}$, $\boldsymbol{X}\succeq\boldsymbol{Y}$ means $\boldsymbol{X}-\boldsymbol{Y}$ is a positive semi-definite matrix. $\mathbb{E}\{\cdot\}$ denotes the expectation operator with respect to (w.r.t.) random variable or vector.

II. SYSTEM MODEL

Consider a wireless network with N mobile agents in the two-dimensional plane.[1] At a given time slot, we model the position of agent i as an unknown deterministic vector $\boldsymbol{x}_i\in\mathbb{R}^2$ for $i=1,2,\dots,N$, and the *actual formation* $\boldsymbol{x}$ of the agents is the vector containing all agent positions, given by

$$\boldsymbol{x}=[\boldsymbol{x}_1^{\mathrm{T}}\quad\boldsymbol{x}_2^{\mathrm{T}}\quad\cdots\quad\boldsymbol{x}_N^{\mathrm{T}}]^{\mathrm{T}}. \tag{1}$$

[1]The analysis can be extended to the three-dimensional case, and the main results hold with minor modifications, as shown in Section III-C.

In this paper, we focus on the analysis for a single time slot, which is divided into the localization phase and the control phase. In the localization phase, the agents make inter-node measurements with each other, and then derive the *formation estimate* $\hat{\mathbf{x}}$ from all the measurements up to the current time slot.[2] In the control phase, the agents depend on the estimated formation $\hat{\mathbf{x}}$ to control their movements collaboratively, in order to form the actual formation as close to the *target formation* as possible, regardless of the formation center and orientation. The target formation $\boldsymbol{\xi}$ is defined as

$$\boldsymbol{\xi} = [\boldsymbol{\xi}_1^{\mathrm{T}} \quad \boldsymbol{\xi}_2^{\mathrm{T}} \quad \cdots \quad \boldsymbol{\xi}_N^{\mathrm{T}}]^{\mathrm{T}} \tag{2}$$

where $\boldsymbol{\xi}_i \in \mathbb{R}^2$ is the position of the ith agent in a target formation.[3] The *MAF design problem* is to achieve the best formation accuracy under resource constraints through optimizing the sensing strategy and the control policy.

A. Measurement Model

Consider all the measurements up to the current time slot denoted by $\mathbf{r} = \{\mathbf{r}^-, \mathbf{d}\}$, where $\mathbf{r}^-$ represents the existing measurements that are gathered in previous time slots, and $\mathbf{d} = \{\mathsf{d}_{ij} : (i,j) \in \mathcal{E}\}$ collects the measurements obtained in the current time slot. Here we denote by (i,j) the measurement link between agent i and j, and by $\mathcal{E}$ the set of all links that can be activated within the current formation.

For simplicity, we consider $\mathbf{d} = \{\mathsf{d}_{ij} : (i,j) \in \mathcal{E}\}$ to be the distance measurements between neighboring nodes through RTT of wireless ranging signals, and the distance measurement between agent i and j is modeled as

$$\mathsf{d}_{ij} = \|\boldsymbol{x}_i - \boldsymbol{x}_j\| + \mathsf{n}_{ij} \tag{3}$$

where the measurement noise $\mathsf{n}_{ij} \sim \mathcal{N}(0, \varsigma_{ij}^2)$ is assumed independent for different inter-node pairs with the variance determined by the spectrum resource allocated to the measurement.

Note that the measurements $\mathbf{r}^-$ are related to the current formation via the state evolution, while the measurements $\mathbf{d}$ directly characterize the network geometry of the current formation. Given the current formation $\boldsymbol{x}$, the two types of the measurements are (conditionally) independent, i.e. $p(\boldsymbol{r};\boldsymbol{x}) = p(\boldsymbol{r}^-;\boldsymbol{x})\,p(\boldsymbol{d};\boldsymbol{x})$. Hence, it follows that the overall Fisher information matrix (FIM) for the current formation can be decomposed as

$$\begin{aligned} \boldsymbol{J}(\boldsymbol{x}) &= \mathbb{E}\big\{[\nabla \ln p(\boldsymbol{r};\boldsymbol{x})][\nabla \ln p(\boldsymbol{r};\boldsymbol{x})]^{\mathrm{T}}\big\} \\ &= \boldsymbol{J}_{\mathrm{A}}(\boldsymbol{x}) + \boldsymbol{J}_{\mathbf{d}}(\boldsymbol{x}) \end{aligned} \tag{4}$$

where $\boldsymbol{J}_{\mathrm{A}}$ and $\boldsymbol{J}_{\mathbf{d}}$ denote the contributions of the existing and current measurements, given by

$$\boldsymbol{J}_{\mathrm{A}}(\boldsymbol{x}) = \mathbb{E}\big\{[\nabla \ln p(\boldsymbol{r}^-;\boldsymbol{x})][\nabla \ln p(\boldsymbol{r}^-;\boldsymbol{x})]^{\mathrm{T}}\big\} \tag{5}$$

$$\boldsymbol{J}_{\mathbf{d}}(\boldsymbol{x}) = \mathbb{E}\big\{[\nabla \ln p(\boldsymbol{d};\boldsymbol{x})][\nabla \ln p(\boldsymbol{d};\boldsymbol{x})]^{\mathrm{T}}\big\} \tag{6}$$

[2]The examples of position related measurements include inter-node distances and directions as well as nodes' velocities and accelerations.

[3]The target formations indeed form a set of vectors because of the translation and rotation operations, and the formation $\boldsymbol{\xi}$ is one element of the target formations. The details will be discussed in Section III-A.

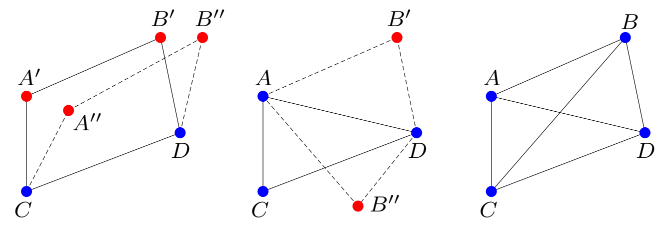

Fig. 2. Examples for rigidness. Given the lengths of all links, the network geometry in (a) and (b) cannot be uniquely determined due to the uncertainty of the agents denoted by red.

respectively. A detailed derivation for $\boldsymbol{J}_{\mathbf{d}}(\boldsymbol{x})$ in general cases can be found in [41], and the results are presented in Appendix A.

Remark 1: To ensure the network geometry can be uniquely determined by the measurements, a sufficient (although not necessary) condition is that the formation with link set $\mathcal{E}$ is *globally rigid* [31]. Generally speaking, if each agent can make measurements with another three agents within the formation, this requirement is satisfied. An example to explain the term is presented in Fig. 2.

B. Control Model

The movement of the agents is composed of the global displacement and local adjustment. The global displacement is common to all agents so that the entire formation moves along a planned trajectory. Since such common movement does not change the geometry of the actual formation, we can assume the global displacement is zero without loss of generality (w.l.o.g.). For the local adjustment, the agents perform local formation control on their movements collaboratively to adjust the actual formation to the target formation.

The control vector on agent i's movement is denoted by $\boldsymbol{c}_i$,[4] and the position of agent i after control is modeled as

$$\mathbf{x}_i^+ = \boldsymbol{x}_i + \boldsymbol{c}_i + \mathbf{w}_i \quad (i = 1, \cdots, N) \tag{7}$$

where the control error $\mathbf{w}_i \sim \mathcal{N}(\mathbf{0}_2, \sigma^2 \boldsymbol{I}_2)$ is assumed i.i.d. for all agents and different time slots. The positions of the agents are random variables due to the uncertainty of the control error. For a compact representation of (7), we define the aggregated vectors for the corresponding terms in the expression: the formation after control, which is called the *posterior formation*, is denoted by $\mathbf{x}^+$; the control vector and error vector for the entire formation are

$$\boldsymbol{c} = [\boldsymbol{c}_1^{\mathrm{T}} \quad \boldsymbol{c}_2^{\mathrm{T}} \quad \cdots \quad \boldsymbol{c}_N^{\mathrm{T}}]^{\mathrm{T}} \tag{8}$$

$$\mathbf{w} = [\mathbf{w}_1^{\mathrm{T}} \quad \mathbf{w}_2^{\mathrm{T}} \quad \cdots \quad \mathbf{w}_N^{\mathrm{T}}]^{\mathrm{T}} \tag{9}$$

respectively.

C. Optimization Formulation

The performance of MAF relies on the accuracy of the position estimates in the network localization procedure. Note

[4]In practical systems, control on the acceleration can be derived by designing the corresponding double-integrator controller [42].

that the localization accuracy of the agents can be significantly improved through optimal allocation of the limited spectrum resource for wireless inter-node measurements [22]. Hence, for MAF applications, it is also desirable to allocate different amount of spectrum resource for different inter-node measurements based on their contributions to the formation performance.

In network localization, two key factors that affect resource allocation are 1) network geometry, and 2) the position uncertainties of the agents and their correlations. In practice, these two factors are described by the estimated positions of the agents $\hat{\mathbf{x}}$, and the FIM of the existing measurements $\boldsymbol{J}_{\mathrm{A}}$ [22].[5] Moreover, there exists a distinct feature in MAF compared to network localization, i.e. the localization errors of different agents have various impacts on the formation performance in view of the target formation $\boldsymbol{\xi}$, as will be shown in Section IV. To conclude, all these three factors need to be taken into account when designing the sensing strategy for the MAF.

Definition 1 (Sensing Strategy): A sensing strategy $\mathscr{S}$ refers to the rule to perform measurements based on the estimated formation $\hat{\mathbf{x}}$, the previous information $\boldsymbol{J}_{\mathrm{A}}$, and the target formation $\boldsymbol{\xi}$, i.e.

$$\mathscr{S}: \ (\hat{\mathbf{x}}, \boldsymbol{J}_{\mathrm{A}}, \boldsymbol{\xi}) \mapsto \mathbf{d}. \tag{10}$$

Once the measurements are obtained, it can provide extra information to estimate the current formation. Most existing studies for formation control determine the control vector based on the estimated formation $\hat{\mathbf{x}}$ and the target formation $\boldsymbol{\xi}$ [32], while ignoring the statistical information in the measurements [43]. Such statistical information can be used to identify the accuracy of the estimated formation and the correlations between the estimation errors of different agents. Therefore, it is beneficial for the MAF performance to leverage the measurements $\mathbf{r}$ when designing the control vector.

Definition 2 (Control Policy): A control policy $\mathscr{C}$ refers to the rule to determine the control vector from the estimated formation $\hat{\mathbf{x}}$, the target formation $\boldsymbol{\xi}$, and all the original distance measurements $\mathbf{r}$, i.e.

$$\mathscr{C}: \ (\hat{\mathbf{x}}, \boldsymbol{\xi}, \mathbf{r}) \mapsto \boldsymbol{c}. \tag{11}$$

Fig. 3 illustrates the ILC scheme, where the sensing strategy and the control policy are jointly designed. In network localization, the goal of MAF, i.e. target formation $\boldsymbol{\xi}$, affects the way of spectrum resource allocation. In formation control, the original measurements are exploited to provide statistical information, such as the confidence of the estimates. Hence, the posterior formation is given by

$$\mathbf{x}^{+} = \boldsymbol{x} + \boldsymbol{c}(\mathbf{r}) + \mathbf{w}. \tag{12}$$

To evaluate the performance of MAF, the next section will present a loss function $\ell(\boldsymbol{x}, \boldsymbol{\xi})$ to characterize the difference between formations $\boldsymbol{x}$ and $\boldsymbol{\xi}$. The goal of this paper is to design the sensing strategy and the control policy that minimizes the expected loss between the posterior formation and the target formation under given spectrum resources, i.e.

$$\begin{aligned} \mathscr{P}: \quad & \underset{\mathscr{S},\mathscr{C}}{\text{minimize}} \quad \mathbb{E}\{\ell(\mathbf{x}^{+}, \boldsymbol{\xi})\} \\ & \text{subject to} \quad \text{spectrum resource } \mathscr{R} \end{aligned} \tag{13}$$

where the expectation is taken over the measurement noises and the control errors.

[5]In this paper, the actual formation $\boldsymbol{x}$ is used for theoretical analysis. Since it is not available in practice, we employ the estimated formation $\hat{\mathbf{x}}$ as a substitute for the actual formation for implementation, e.g. in Algorithm 1 and the equations therein.

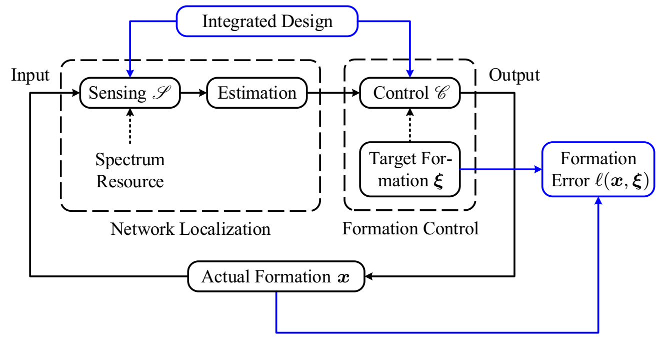

Fig. 3. The flow diagram of the ILC scheme. This scheme employs the proposed formation error as the performance metric, which quantifies the difference between the actual and target formations. In addition, the ILC scheme designs the network localization and the formation control procedures in an integrated way by 1) taking the target formation into account in the sensing strategy, and 2) using the original measurements when determining the control vector.

III. Performance Metric

In this section, we propose a new metric (formation error) to characterize the difference between the actual formation and the target one, which is the minimum squared distance between the two formations for arbitrary translation and rotation.

A. Formation Distance

In a wide range of applications carried out by multi-agent systems, only the geometry of the actual formation is relevant. In this context, two formations are considered *equivalent* if they can be transformed into each other through translations and rotations. The conventional squared localization errors cannot fully characterize the difference between two formations in this sense, and a new performance metric, which is invariant to the translation and rotation operators, is proposed in this section. First of all, we define the equivalent formation set as the collection of all equivalent formations in terms of network geometry, which is recognized in the literatures of relative localization [24] and formation control [31].

Definition 3 (Equivalent Formation Set): The set that contains all the formations equivalent to the formation $\boldsymbol{q}$ is called the equivalent formation set of $\boldsymbol{q}$, denoted by $\mathcal{F}(\boldsymbol{q})$. Its subset that collects all the formations centered at the origin is called the *basic equivalent formation set*, denoted by $\mathcal{F}^0(\boldsymbol{q})$.

According to Definition 3, the equivalent formation set of a two-dimensional formation $\boldsymbol{q}$ can be expressed as

$$\mathcal{F}(\boldsymbol{q}) = \left\{ \boldsymbol{G}(\vartheta)\boldsymbol{q} + \mathbf{1}_N \otimes \boldsymbol{k} \, : \, \boldsymbol{k} \in \mathbb{R}^2, \vartheta \in [0, 2\pi) \right\} \tag{14}$$

where $\boldsymbol{G}(\vartheta)=\boldsymbol{I}_N\otimes\boldsymbol{G}_2(\vartheta)$ with the rotation matrix

$$\boldsymbol{G}_2(\vartheta)=\begin{bmatrix}\cos\vartheta & -\sin\vartheta\\ \sin\vartheta & \cos\vartheta\end{bmatrix} \tag{15}$$

and $\otimes$ denotes the Kronecker product. In other words, the elements in the equivalent formation set are obtained by rotating the entire formation $\boldsymbol{q}$ by angle ϑ and then translating the resulting formation by vector $\boldsymbol{k}$. We can observe from (14) that given the formation $\boldsymbol{q}$, its equivalent formation set has three dimensions of freedom, with two accounting for translation and the other one for rotation. Hence, the dimension of the set $\mathcal{F}=\{\mathcal{F}(\boldsymbol{s}):\boldsymbol{s}\in\mathbb{R}^{2N}\}$ is $2N-3$.

Next, we derive the expression for the basic equivalent formation set. We first define that

$$\boldsymbol{D}=\frac{1}{N}\big(\boldsymbol{d}_x\boldsymbol{d}_x^{\mathrm{T}}+\boldsymbol{d}_y\boldsymbol{d}_y^{\mathrm{T}}\big) \tag{16}$$

where $\boldsymbol{d}_x=\boldsymbol{1}_N\otimes[1\quad 0]^{\mathrm{T}}$ and $\boldsymbol{d}_y=\boldsymbol{1}_N\otimes[0\quad 1]^{\mathrm{T}}$. For a general formation $\boldsymbol{q}$, $\boldsymbol{D}\boldsymbol{q}=\boldsymbol{1}_N\otimes\boldsymbol{q}_{\mathrm{c}}$ with $\boldsymbol{q}_{\mathrm{c}}$ representing the center of the formation $\boldsymbol{q}$. As a result, the *basic formation* $\widetilde{\boldsymbol{q}}$, which is the coordinate of the formation $\boldsymbol{q}$ in its center-of-mass reference frame, is given by

$$\widetilde{\boldsymbol{q}}=(\boldsymbol{I}-\boldsymbol{D})\boldsymbol{q}. \tag{17}$$

One can verify that the formation $\widetilde{\boldsymbol{q}}$ centers at the origin. With the centers fixed, the formations in $\mathcal{F}^0(\boldsymbol{q})$ can only be equivalent to each other by rotation, and it indicates that

$$\mathcal{F}^0(\boldsymbol{q})=\big\{\boldsymbol{G}(\vartheta)(\boldsymbol{I}-\boldsymbol{D})\boldsymbol{q}\,:\,\vartheta\in[0,2\pi)\big\}. \tag{18}$$

which has only one dimension of freedom.[6]

Definition 4 (Formation Distance): The formation distance between $\boldsymbol{p}$ and $\boldsymbol{q}$ is the Euclidean distance between the equivalent formation sets $\mathcal{F}(\boldsymbol{p})$ and $\mathcal{F}(\boldsymbol{q})$, defined as[7]

$$d(\boldsymbol{p},\boldsymbol{q})=\min_{\boldsymbol{s}\in\mathcal{F}(\boldsymbol{p}),\ \boldsymbol{t}\in\mathcal{F}(\boldsymbol{q})}\|\boldsymbol{s}-\boldsymbol{t}\|. \tag{19}$$

The above optimization problem can be solved analytically, leading to a closed-form expression for $d(\boldsymbol{p},\boldsymbol{q})$ shown in the following proposition.

Proposition 1: The formation distance between formations $\boldsymbol{p}$ and $\boldsymbol{q}$ is given by

$$d(\boldsymbol{p},\boldsymbol{q})=\Big(\|\widetilde{\boldsymbol{p}}\|^2+\|\widetilde{\boldsymbol{q}}\|^2-2\|\widetilde{\boldsymbol{q}}\|\sqrt{\widetilde{\boldsymbol{p}}^{\mathrm{T}}\boldsymbol{Q}\widetilde{\boldsymbol{p}}}\Big)^{1/2} \tag{20}$$

where

$$\boldsymbol{Q}=\|\widetilde{\boldsymbol{q}}\|^{-2}(\widetilde{\boldsymbol{q}}\widetilde{\boldsymbol{q}}^{\mathrm{T}}+\widetilde{\boldsymbol{q}}_\perp\widetilde{\boldsymbol{q}}_\perp^{\mathrm{T}}) \tag{21}$$

with $\widetilde{\boldsymbol{q}}_\perp=\boldsymbol{R}\widetilde{\boldsymbol{q}}$ in which $\boldsymbol{R}=\boldsymbol{G}(\pi/2)$.

Proof: See Appendix B. □

Note that the equivalent formation sets generated by equivalent formations are unique, and the formation distance is defined for two equivalent formation sets, which indicates that the formation distances calculated by equivalent pairs of formations are equal.[8] The property is verified in the following proposition.

Proposition 2: For any formations $\boldsymbol{p}_{\mathrm{e}}\in\mathcal{F}(\boldsymbol{p})$ and $\boldsymbol{q}_{\mathrm{e}}\in\mathcal{F}(\boldsymbol{q})$, the formation distance between $\boldsymbol{p}_{\mathrm{e}}$ and $\boldsymbol{q}_{\mathrm{e}}$ is given by

$$d(\boldsymbol{p}_{\mathrm{e}},\boldsymbol{q}_{\mathrm{e}})=d(\boldsymbol{p},\boldsymbol{q}). \tag{22}$$

Proof: Assume w.l.o.g. that all the related formations, i.e. $\boldsymbol{p}$, $\boldsymbol{p}_{\mathrm{e}}$, $\boldsymbol{q}$ and $\boldsymbol{q}_{\mathrm{e}}$ are centered at the origin. Then according to definition (18), we have

$$\boldsymbol{p}_{\mathrm{e}}=\boldsymbol{G}(\vartheta)\boldsymbol{p}=[\,\boldsymbol{p}\quad\boldsymbol{R}\boldsymbol{p}\,]\boldsymbol{u}(\vartheta) \tag{23}$$

for some ϑ with $\boldsymbol{u}(\vartheta)=[\cos\vartheta\quad\sin\vartheta]^{\mathrm{T}}$. It follows that

$$\|\boldsymbol{p}_{\mathrm{e}}\|=\|\boldsymbol{p}\| \tag{24}$$

since $\|\boldsymbol{p}\|=\|\boldsymbol{R}\boldsymbol{p}\|$ and $\boldsymbol{p}^{\mathrm{T}}(\boldsymbol{R}\boldsymbol{p})=0$; and

$$\begin{aligned}
&\|\boldsymbol{q}\|^2\big(\boldsymbol{p}_{\mathrm{e}}^{\mathrm{T}}\boldsymbol{Q}\boldsymbol{p}_{\mathrm{e}}\big)=\big(\boldsymbol{p}_{\mathrm{e}}^{\mathrm{T}}\boldsymbol{q}\big)^2+\big(\boldsymbol{p}_{\mathrm{e}}^{\mathrm{T}}\boldsymbol{R}\boldsymbol{q}\big)^2\\
&=\left(\boldsymbol{u}(\alpha)^{\mathrm{T}}\begin{bmatrix}\boldsymbol{p}^{\mathrm{T}}\boldsymbol{q}\\ \boldsymbol{p}^{\mathrm{T}}\boldsymbol{R}^{T}\boldsymbol{q}\end{bmatrix}\right)^2+\left(\boldsymbol{u}(\alpha)^{\mathrm{T}}\begin{bmatrix}\boldsymbol{p}^{\mathrm{T}}\boldsymbol{R}\boldsymbol{q}\\ \boldsymbol{p}^{\mathrm{T}}\boldsymbol{R}^{T}\boldsymbol{R}\boldsymbol{q}\end{bmatrix}\right)^2\\
&=\left(\boldsymbol{u}(\alpha)^{\mathrm{T}}\begin{bmatrix}\boldsymbol{p}^{\mathrm{T}}\boldsymbol{q}\\ -\boldsymbol{p}^{\mathrm{T}}\boldsymbol{R}\boldsymbol{q}\end{bmatrix}\right)^2+\left(\boldsymbol{u}(\alpha)^{\mathrm{T}}\begin{bmatrix}\boldsymbol{p}^{\mathrm{T}}\boldsymbol{R}\boldsymbol{q}\\ \boldsymbol{p}^{\mathrm{T}}\boldsymbol{q}\end{bmatrix}\right)^2\\
&=\big(\boldsymbol{p}^{\mathrm{T}}\boldsymbol{q}\big)^2+\big(\boldsymbol{p}^{\mathrm{T}}\boldsymbol{R}\boldsymbol{q}\big)^2=\|\boldsymbol{q}\|^2\big(\boldsymbol{p}^{\mathrm{T}}\boldsymbol{Q}\boldsymbol{p}\big)
\end{aligned} \tag{25}$$

or equivalently

$$\boldsymbol{p}_{\mathrm{e}}^{\mathrm{T}}\boldsymbol{Q}\boldsymbol{p}_{\mathrm{e}}=\boldsymbol{p}^{\mathrm{T}}\boldsymbol{Q}\boldsymbol{p} \tag{26}$$

where the third equality in (25) holds since $\boldsymbol{R}^{\mathrm{T}}=-\boldsymbol{R}$ and $\boldsymbol{R}^{\mathrm{T}}\boldsymbol{R}=\boldsymbol{I}$. Substituting (24) and (26) into (20) leads to $d(\boldsymbol{p},\boldsymbol{q})=d(\boldsymbol{p}_{\mathrm{e}},\boldsymbol{q})$. Finally, since the formation distance is symmetric by Definition 4, it follows that $d(\boldsymbol{p},\boldsymbol{q})=d(\boldsymbol{p}_{\mathrm{e}},\boldsymbol{q})=d(\boldsymbol{q},\boldsymbol{p}_{\mathrm{e}})=d(\boldsymbol{q}_{\mathrm{e}},\boldsymbol{p}_{\mathrm{e}})=d(\boldsymbol{p}_{\mathrm{e}},\boldsymbol{q}_{\mathrm{e}})$. □

In the following proposition, we show three properties of the proposed formation distance. Again, we emphasize that the metric function $d(\cdot,\cdot)$ is defined on $\mathcal{F}\times\mathcal{F}$.

Proposition 3: The formation distance $d(\boldsymbol{p},\boldsymbol{q})$ is a metric on $\mathcal{F}=\{\mathcal{F}(\boldsymbol{s}):\boldsymbol{s}\in\mathbb{R}^{2N}\}$, i.e. $d(\boldsymbol{p},\boldsymbol{q})$ satisfies the properties of identity of indiscernibles, symmetry, and triangle inequality.

Proof: See Appendix C. □

Proposition 1 implies that the formation distance between two formations is only related to the corresponding formations in the basic equivalent formation sets. Therefore, in the rest of the paper, we can assume the formations centered at the origin w.l.o.g. and use the notation $\boldsymbol{p}$ for $\widetilde{\boldsymbol{p}}$ for simplicity.

B. Formation Error

Based on the proposed formation distance, we can further define the formation error to characterize the difference between the actual formation and the target formation.

Definition 5 (Formation Error): The formation error between the actual formation $\boldsymbol{x}$ and the target formation $\boldsymbol{\xi}$ is defined as the squared formation distance between them, i.e.

$$\ell(\boldsymbol{x},\boldsymbol{\xi})=d(\boldsymbol{x},\boldsymbol{\xi})^2. \tag{27}$$

[6] The above definitions for $\boldsymbol{q}_{\mathrm{c}}$, $\widetilde{\boldsymbol{q}}$ and $\mathcal{F}^0(\boldsymbol{q})$ apply to all formations.

[7] Note that we slightly abuse the notation $d(\boldsymbol{p},\boldsymbol{q})$ for simplicity. Strictly speaking, the formation distance function is defined on $\mathcal{F}\times\mathcal{F}$, i.e. it is w.r.t. two equivalent formation sets $\mathcal{F}(\boldsymbol{p})$ and $\mathcal{F}(\boldsymbol{q})$, denoted by $d(\mathcal{F}(\boldsymbol{p}),\mathcal{F}(\boldsymbol{q}))$.

[8] Two pairs of formations are called equivalent if all the corresponding entries are equivalent formations.

The formation error can be interpreted as the least cost of control to form the actual formation as the target formation.[9] Substitute (20) into the above definition, and the formation error can be obtained in a closed-form expression as

$$\ell(\boldsymbol{x},\boldsymbol{\xi}) = \|\boldsymbol{x}\|^2 + \|\boldsymbol{\xi}\|^2 - 2\|\boldsymbol{\xi}\|\sqrt{\boldsymbol{x}^{\mathrm{T}}\boldsymbol{\varXi}\boldsymbol{x}} \tag{28}$$

where

$$\boldsymbol{\varXi} = \|\boldsymbol{\xi}\|^{-2}(\boldsymbol{\xi}\boldsymbol{\xi}^{\mathrm{T}} + \boldsymbol{\eta}\boldsymbol{\eta}^{\mathrm{T}}) \tag{29}$$

with $\boldsymbol{\eta} = \boldsymbol{R}\boldsymbol{\xi}$. Note that $\boldsymbol{\eta}$ is another target formation that can be achieved by rotating the formation $\boldsymbol{\xi}$ by $\vartheta = \pi/2$, and it follows that $\|\boldsymbol{\eta}\| = \|\boldsymbol{\xi}\|$ and $\boldsymbol{\xi}^{\mathrm{T}}\boldsymbol{\eta} = 0$. Thus, $\boldsymbol{\varXi}$ is a projection matrix, which denotes the operation that projects a formation of N agents into the subspace

$$\mathcal{P} := \operatorname{span}\{\boldsymbol{\xi}, \boldsymbol{\eta}\} \tag{30}$$

where $\{\boldsymbol{\xi}, \boldsymbol{\eta}\}$ forms a set of orthogonal basis.

Proposition 4: The basic equivalent formation set of the target formation $\boldsymbol{\xi}$ is the set of points lying on the circle of radius $\|\boldsymbol{\xi}\|$ centered at the origin in the hyperplane $\mathcal{P}$.

Proof: For a target formation $\boldsymbol{\zeta}$ centered at the origin, i.e. $\boldsymbol{\zeta} \in \mathcal{F}^0(\boldsymbol{\xi})$, according to (18), it can be expressed as

$$\boldsymbol{\zeta} = \boldsymbol{G}(\vartheta)\boldsymbol{\xi} = \left[\cos(\vartheta)\boldsymbol{I} + \sin(\vartheta)\boldsymbol{R}\right]\boldsymbol{\xi} = \begin{bmatrix}\boldsymbol{\xi} & \boldsymbol{\eta}\end{bmatrix}\boldsymbol{u}(\vartheta). \tag{31}$$

Thus, $\boldsymbol{\zeta} \in \mathcal{P}$ and $\|\boldsymbol{\zeta}\| = \|\boldsymbol{\xi}\|$, and vice versa. □

An equivalent form for the formation error is derived from the perspective of subspaces in the next proposition, followed by a geometrical interpretation.

Proposition 5: The formation error can be decomposed as

$$\ell(\boldsymbol{x},\boldsymbol{\xi}) = \|\boldsymbol{x}_\perp\|^2 + \left(\|\boldsymbol{x}_{/\!/}\| - \|\boldsymbol{\xi}\|\right)^2 \tag{32}$$

where $\boldsymbol{x}_{/\!/} = \boldsymbol{\varXi}\boldsymbol{x}$ and $\boldsymbol{x}_\perp = (\boldsymbol{I} - \boldsymbol{\varXi})\boldsymbol{x}$ are the components of the formation $\boldsymbol{x}$ in the subspace $\mathcal{P}$ and its orthogonal complementary $\mathcal{P}^\perp$, respectively.

Proof: By the orthogonal projection theorem, the formation $\boldsymbol{x}$ can be decomposed as $\boldsymbol{x}_{/\!/}$ within the range and $\boldsymbol{x}_\perp$ within the kernel of the projection matrix $\boldsymbol{\varXi}$. It follows that

$$\|\boldsymbol{x}\|^2 = \|\boldsymbol{x}_{/\!/}\|^2 + \|\boldsymbol{x}_\perp\|^2. \tag{33}$$

Since $\boldsymbol{\varXi}$ is both symmetric and idempotent, we have

$$\boldsymbol{x}^{\mathrm{T}}\boldsymbol{\varXi}\boldsymbol{x} = [\boldsymbol{\varXi}\boldsymbol{x}]^{\mathrm{T}}[\boldsymbol{\varXi}\boldsymbol{x}] = \|\boldsymbol{x}_{/\!/}\|^2. \tag{34}$$

Substituting the above terms into (28) leads to (32). □

Proposition 5 shows that the formation error can be decomposed as the *orthogonal error* and the *parallel error*, as shown in Fig. 4. The orthogonal error is the squared distance from the formation to the hyperplane $\mathcal{P}$, and the parallel error is the squared distance from the projection $\boldsymbol{x}_{/\!/}$ to the circle of target formations. Note that the rotation of the formation is irrelevant in the formation error, since the target formation with different rotations generates a circle in the plane $\mathcal{P}$.

Remark 2: Recall that the formations are assumed to be centered at origin, or otherwise one can take $\widetilde{\boldsymbol{x}} = (\boldsymbol{I} - \boldsymbol{D})\boldsymbol{x}$ instead of $\boldsymbol{x}$. From the perspective of subspaces, $\boldsymbol{D}$ is also a projection matrix that projects a formation into the subspace

$$\mathcal{D} := \operatorname{span}\{\boldsymbol{d}_x, \boldsymbol{d}_y\}\,. \tag{35}$$

Furthermore, the two subspaces are orthogonal, i.e. $\mathcal{D} \perp \mathcal{P}$, since $\boldsymbol{\xi}^{\mathrm{T}}\boldsymbol{d}_x = \boldsymbol{\xi}^{\mathrm{T}}\boldsymbol{d}_y = \boldsymbol{\eta}^{\mathrm{T}}\boldsymbol{d}_x = \boldsymbol{\eta}^{\mathrm{T}}\boldsymbol{d}_y = 0$, and the entire space in Fig. 3 is the complementary subspace of $\mathcal{D}$.

[9] In this paper, the cost of control refers to the sum of squared distances that each agent moves during the formation control procedure.

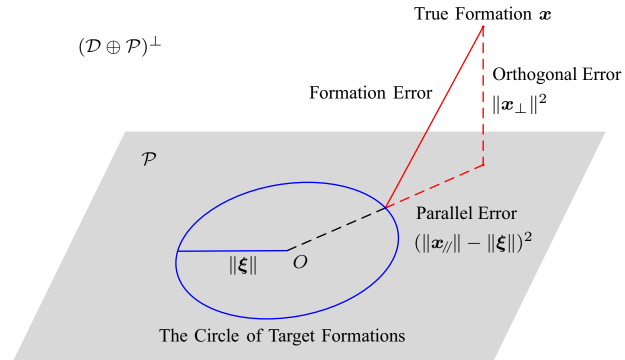

Fig. 4. Geometrical interpretation: The target formation is represented by a circle with radius $\|\boldsymbol{\xi}\|$ in $\mathcal{P}$, and the formation error can be decomposed as the sum of the parallel error in $\mathcal{P}$ and the orthogonal error in $(\mathcal{D} \oplus \mathcal{P})^\perp$, where $\mathcal{P} = \operatorname{span}\{\boldsymbol{\xi}, \boldsymbol{\eta}\}$, $\mathcal{D} = \operatorname{span}\{\boldsymbol{d}_x, \boldsymbol{d}_y\}$, and $\oplus$ denotes the sum of subspaces. Note that the entire space in this figure is $\mathcal{D}^\perp$ of dimension $2N-2$.

C. Extensions of Formation Error

1) Scalable Formations: In scenarios where only the angle measurements between the agents are available [24], a formation that can be achieved by scaling some target formation is also regarded as a target formation. In this case, the equivalent formation set of the target formation $\boldsymbol{\xi}$ is defined as

$$\mathcal{F}_{\mathrm{s}}(\boldsymbol{\xi}) = \{\beta\boldsymbol{s} + \boldsymbol{1}_N \otimes \boldsymbol{k} \,:\, \boldsymbol{s} \in \mathcal{F}^0(\boldsymbol{\xi}), \beta \in \mathbb{R}\}. \tag{36}$$

Following the definition for the formation error, we can derive a closed-form expression for scalable formations in an analogous way. We next present another method to derive the formation error, which leverages the insights of the geometrical interpretation and the perspective of subspaces.

Proposition 6: For scalable target formations, the formation error is only composed of the orthogonal error, i.e.

$$\ell_{\mathrm{s}}(\boldsymbol{x},\boldsymbol{\xi}) = \|(\boldsymbol{I} - \boldsymbol{\varXi})\boldsymbol{x}\|^2. \tag{37}$$

Proof: As shown in Proposition 4, the basic equivalent formation set $\mathcal{F}^0$ forms the target circle, and it can be proved that the basic equivalent formation set in the scalable case $\mathcal{F}^0_{\mathrm{s}}$ is the subspace $\mathcal{P}$. First, we show that $\mathcal{F}^0_{\mathrm{s}} \in \mathcal{P}$: since $\forall \boldsymbol{\iota} \in \mathcal{F}^0_{\mathrm{s}}$ has the form of $\boldsymbol{\iota} = \beta\boldsymbol{s}$ for some $\beta \in \mathbb{R}$ and $\boldsymbol{s} \in \mathcal{F}^0(\boldsymbol{\xi}) \in \mathcal{P}$, it follows that $\boldsymbol{\iota} \in \mathcal{P}$; then we show that $\mathcal{P} \in \mathcal{F}^0_{\mathrm{s}}$, and the proof is an inverse to the previous procedure.

Thus, the parallel error vanishes, and the formation error is equal to its orthogonal part as shown in (37). □

2) Three-dimensional Formations: In aerial or marine scenarios, the target formations usually can be rotated around a given axis in the space, typically the vertical axis. The matrix that rotates a formation $\boldsymbol{x} \in \mathbb{R}^{3N}$ around an unit axis $\boldsymbol{z} = [z_1 \quad z_2 \quad z_3]^{\mathrm{T}}$ by ϑ is given by

$$\boldsymbol{G}_{\boldsymbol{z}}(\vartheta) = \boldsymbol{I}_{3N} + (\sin\vartheta)\boldsymbol{Z} + (1-\cos\vartheta)\boldsymbol{Z}^2 \tag{38}$$

where $\boldsymbol{Z}$ is the extended cross product matrix of $\boldsymbol{z}$, i.e.

$$\boldsymbol{Z} = \boldsymbol{I}_N \otimes \begin{bmatrix} 0 & -z_3 & z_2 \\ z_3 & 0 & -z_1 \\ -z_2 & z_1 & 0 \end{bmatrix}. \tag{39}$$

Thus, the equivalent formation set of the target formation $\boldsymbol{\xi}$ is

$$\begin{aligned} \mathcal{F}_3(\boldsymbol{\xi}) &= \{\boldsymbol{G}_{\boldsymbol{z}}(\vartheta)\boldsymbol{\xi} + \mathbf{1}_N \otimes \boldsymbol{k} \,:\, \boldsymbol{k} \in \mathbb{R}^3, \vartheta \in [0, 2\pi)\} \\ &= \{(\sin\vartheta)\,\boldsymbol{Z}\boldsymbol{\xi} + (\cos\vartheta)\,\boldsymbol{Z}^2\boldsymbol{\xi} + \mathbf{1}_N \otimes \boldsymbol{k} \\ &\qquad : \boldsymbol{k} \in \mathbb{R}^3, \vartheta \in [0, 2\pi)\}. \end{aligned} \tag{40}$$

It can be shown that the basis $\{\boldsymbol{Z}\boldsymbol{\xi}, \boldsymbol{Z}^2\boldsymbol{\xi}\}$ are orthogonal to each other since $(\boldsymbol{Z}\boldsymbol{\xi})^{\mathrm{T}}(\boldsymbol{Z}^2\boldsymbol{\xi}) = -\boldsymbol{\xi}^{\mathrm{T}}\boldsymbol{Z}\boldsymbol{\xi} = 0$, and

$$\|\boldsymbol{Z}\boldsymbol{\xi}\| = \|\boldsymbol{Z}^2\boldsymbol{\xi}\| = \sqrt{\|\boldsymbol{\xi}\|^2 - (\boldsymbol{\xi}^{\mathrm{T}}\boldsymbol{z})^2}. \tag{41}$$

The equivalent formation set for three-dimensional formations (40) is the same with (14) except a minor difference in the definition of the basis. Thus, the formation error is given by

$$\ell_3(\boldsymbol{x}, \boldsymbol{\xi}) = \|(\boldsymbol{I}_{3N} - \boldsymbol{\varXi}_3)\boldsymbol{x}\|^2 + (\|\boldsymbol{\varXi}_3\boldsymbol{x}\| - \|\boldsymbol{Z}\boldsymbol{\xi}\|)^2 \tag{42}$$

where

$$\boldsymbol{\varXi}_3 = \|\boldsymbol{Z}\boldsymbol{\xi}\|^{-2}(-\boldsymbol{Z}\boldsymbol{\xi}\boldsymbol{\xi}^{\mathrm{T}}\boldsymbol{Z} + \boldsymbol{Z}^2\boldsymbol{\xi}\boldsymbol{\xi}^{\mathrm{T}}\boldsymbol{Z}^2). \tag{43}$$

Similar to Proposition 4, all the target formations centered at the origin form a circle of radius $\|\boldsymbol{Z}\boldsymbol{\xi}\|$ in the hyperplane $\mathcal{P}_3 = \mathrm{span}\{\boldsymbol{Z}\boldsymbol{\xi}, \boldsymbol{Z}^2\boldsymbol{\xi}\}$ in the three-dimensional case.

IV. Theoretical Bounds for MFE

In this section, we first define the MFE to characterize the performance of MAF for random formations, and then derive the upper and lower bounds for the MFE.

A. MFE for Random Formations

Recall the posterior formation given in (12). Due to the measurement noises and the control errors, the posterior formation is a random vector. Thus, we extend the formation error metric to this stochastic case, and define MFE to characterize the mean performance of MAF for a random formation.

Definition 6 (MFE): The MFE between a random formation x and the target formation $\boldsymbol{\xi}$ is given by

$$\bar{\ell} = \mathbb{E}_{\mathsf{x}}\{\ell(\mathsf{x}, \boldsymbol{\xi})\}. \tag{44}$$

Since the formation error can be decomposed as (32) and the expectation operator is linear, the MFE for the posterior formation can be written as

$$\bar{\ell} = \bar{\ell}_{\perp} + \bar{\ell}_{/\!/} \tag{45}$$

where $\bar{\ell}_{\perp}$ and $\bar{\ell}_{/\!/}$ are called the expected orthogonal error and the expected parallel error, given respectively by

$$\bar{\ell}_{\perp} = \mathbb{E}_{\mathsf{r}, \mathsf{w}_{\perp}}\left\{\|\boldsymbol{x}_{\perp} + \boldsymbol{c}_{\perp}(\mathsf{r}) + \mathsf{w}_{\perp}\|^2\right\} \tag{46}$$

$$\bar{\ell}_{/\!/} = \mathbb{E}_{\mathsf{r}, \mathsf{w}_{/\!/}}\left\{(\|\boldsymbol{x}_{/\!/} + \boldsymbol{c}_{/\!/}(\mathsf{r}) + \mathsf{w}_{/\!/}\| - \|\boldsymbol{\xi}\|)^2\right\} \tag{47}$$

in which $\boldsymbol{c}_{\perp}$ and $\boldsymbol{c}_{/\!/}$ are the components of the control policy $\boldsymbol{c}$ in the subspace $(\mathcal{D} \oplus \mathcal{P})^{\perp}$ and $\mathcal{P}$; $\mathsf{w}_{\perp} = (\boldsymbol{I} - \boldsymbol{D} - \boldsymbol{\varXi})\mathsf{w}$ and $\mathsf{w}_{/\!/} = \boldsymbol{\varXi}\mathsf{w}$ are the components of the aggregated control error w.

Recall that the control error w follows a Gaussian distribution, we can verify that

$$\begin{bmatrix} \mathsf{w}_{\perp} \\ \mathsf{w}_{/\!/} \end{bmatrix} \sim \mathcal{N}\left(\mathbf{0}_{4N}, \sigma^2 \begin{bmatrix} \boldsymbol{I} - \boldsymbol{D} - \boldsymbol{\varXi} & \boldsymbol{O} \\ \boldsymbol{O} & \boldsymbol{\varXi} \end{bmatrix}\right). \tag{48}$$

In other word, the components of the control error in both subspaces, i.e. $\mathsf{w}_{\perp}$ and $\mathsf{w}_{/\!/}$, are independent. Combining with the fact that the error components $\bar{\ell}_{\perp}$ and $\bar{\ell}_{/\!/}$ contribute to the MFE in an uncorrelated manner (45), we are allowed to design the control policies $\boldsymbol{c}_{\perp}$ and $\boldsymbol{c}_{/\!/}$ in the two subspaces separately.

Definition 7 (MFEB): The mean formation error bound (MFEB) F is the lower bound for the MFE by the optimal position estimation and control vector, i.e.

$$F = \min_{\boldsymbol{c}} \bar{\ell}. \tag{49}$$

Since the MFE can be decomposed as (45) and the control policies can be designed separately, the MFEB can be decomposed as

$$F = F_{\perp} + F_{/\!/} \tag{50}$$

where

$$F_{\perp} = \min_{\boldsymbol{c}_{\perp}} \bar{\ell}_{\perp} \quad \text{and} \quad F_{/\!/} = \min_{\boldsymbol{c}_{/\!/}} \bar{\ell}_{/\!/} \tag{51}$$

are called the expected orthogonal error bound and the expected parallel error bound, respectively.

B. Bounds for the MFEB

In light of (50) and (51), we will first derive each part of the MFEB, as well as the components of the control policy in the subspaces; then a unified theorem presenting the overall MFEB and the corresponding control policy is provided.

1) Expected Orthogonal Error Bound: Since the measurement noises and the control errors are assumed independent, the expected orthogonal error in (46) can be simplified as

$$\bar{\ell}_{\perp} = \mathbb{E}_{\mathsf{r}}\{\|\boldsymbol{x}_{\perp} + \boldsymbol{c}_{\perp}(\mathsf{r})\|^2\} + (2N-4)\sigma^2. \tag{52}$$

The following proposition presents the form of the expected orthogonal error bound.

Proposition 7: For arbitrary control policies, the expected orthogonal error $\bar{\ell}_{\perp}$ is lower bounded by

$$F_{\perp} = \mathrm{tr}\left\{(\boldsymbol{I} - \boldsymbol{D} - \boldsymbol{\varXi})\boldsymbol{J}(\boldsymbol{x})^{-1}\right\} + (2N-4)\sigma^2 \tag{53}$$

where $\boldsymbol{J}(\boldsymbol{x})$ is the FIM of the actual formation $\boldsymbol{x}$, given by (4). The lower bound is achieved under the control policy

$$\boldsymbol{c}_{\perp}^{\star}(\boldsymbol{r}) = -(\boldsymbol{I} - \boldsymbol{D} - \boldsymbol{\varXi})\boldsymbol{J}(\boldsymbol{x})^{-1}\nabla \ln p(\boldsymbol{r}; \boldsymbol{x}) - \boldsymbol{x}_{\perp}. \tag{54}$$

Proof: See Appendix D-A. □

The orthogonal error is related to the component $\mathsf{x}_{\perp}^{+}$ in the subspace $(\mathcal{D} \oplus \mathcal{P})^{\perp}$. In (53), the first term corresponds to the projection of the localization error characterized by $\mathrm{tr}\left\{\boldsymbol{J}(\boldsymbol{x})^{-1}\right\}$ into this subspace; and the second term represents the control error in this subspace, and the coefficient $2N-4$ is due to the fact that $\dim(\mathcal{D} \oplus \mathcal{P})^{\perp} = 2N-4$.

2) Expected Parallel Error Bound: In this section, we will first derive the upper bound for the expected parallel error bound $F_{/\!/}$. For any given observation vector $\boldsymbol{r}$, the random variable $\|\boldsymbol{x}_{/\!/}+\boldsymbol{c}_{/\!/}(\boldsymbol{r})+\mathbf{w}_{/\!/}\|$ follows the Rician distribution.[10] It follows that its mean value satisfies

$$\mathbb{E}_{\mathbf{w}_{/\!/}}\{\|\boldsymbol{x}_{/\!/}+\boldsymbol{c}_{/\!/}(\boldsymbol{r})+\mathbf{w}_{/\!/}\|\}\geq\|\boldsymbol{x}_{/\!/}+\boldsymbol{c}_{/\!/}(\boldsymbol{r})\|. \tag{55}$$

Applying the above inequality to (47), we can obtain

$$\begin{aligned}\bar{\ell}_{/\!/}&=\mathbb{E}_{\mathbf{r}}\left\{\|\boldsymbol{x}_{/\!/}+\boldsymbol{c}_{/\!/}(\mathbf{r})\|^2\right\}+\mathbb{E}_{\mathbf{w}_{/\!/}}\left\{\mathbf{w}_{/\!/}^{\mathrm{T}}\mathbf{w}_{/\!/}\right\}+\|\boldsymbol{\xi}\|^2\\&\quad-2\|\boldsymbol{\xi}\|\,\mathbb{E}_{\mathbf{r}}\left\{\mathbb{E}_{\mathbf{w}_{/\!/}}\left\{\|\boldsymbol{x}_{/\!/}+\boldsymbol{c}_{/\!/}(\mathbf{r})+\mathbf{w}_{/\!/}\|\,|\,\mathbf{r}\right\}\right\}\\&\leq\mathbb{E}_{\mathbf{r}}\{(\|\boldsymbol{x}_{/\!/}+\boldsymbol{c}_{/\!/}(\mathbf{r})\|-\|\boldsymbol{\xi}\|)^2\}+2\sigma^2\end{aligned} \tag{56}$$

for any control policy $\boldsymbol{c}_{/\!/}$. It follows that

$$0\leq F_{/\!/}\leq\underbrace{\min_{\boldsymbol{c}_{/\!/}}\mathbb{E}_{\mathbf{r}}\{(\|\boldsymbol{x}_{/\!/}+\boldsymbol{c}_{/\!/}(\mathbf{r})\|-\|\boldsymbol{\xi}\|)^2\}}_{L_{/\!/}}+2\sigma^2 \tag{57}$$

where $L_{/\!/}$ accounts for the effect of the measurement noise on the expected parallel error.

Proposition 8: For arbitrary control policies, the upper bound of the the expected parallel error bound is given by $\overline{F_{/\!/}}=L_{/\!/}+2\sigma^2$ with

$$L_{/\!/}=\mathrm{tr}\left\{\left(\frac{\boldsymbol{\Xi}}{2}\right)\boldsymbol{J}(\boldsymbol{x})^{-1}\right\}-\frac{1}{2}\left\|\begin{bmatrix}\mathrm{tr}\left\{\boldsymbol{P}_1\boldsymbol{J}(\boldsymbol{x})^{-1}\right\}\\\mathrm{tr}\left\{\boldsymbol{P}_2\boldsymbol{J}(\boldsymbol{x})^{-1}\right\}\end{bmatrix}\right\| \tag{58}$$

with $\boldsymbol{P}_1=\|\boldsymbol{\xi}\|^{-2}(\boldsymbol{\xi}\boldsymbol{\xi}^{\mathrm{T}}-\boldsymbol{\eta}\boldsymbol{\eta}^{\mathrm{T}})$ and $\boldsymbol{P}_2=\|\boldsymbol{\xi}\|^{-2}(\boldsymbol{\xi}\boldsymbol{\eta}^{\mathrm{T}}+\boldsymbol{\eta}\boldsymbol{\xi}^{\mathrm{T}})$. The upper bound is achieved under the control policy

$$\boldsymbol{c}_{/\!/}^{\star}(\boldsymbol{r})=-\left[\|\boldsymbol{\xi}\|+\nabla\ln p(\boldsymbol{r};\boldsymbol{x})^{\mathrm{T}}\boldsymbol{J}(\boldsymbol{x})^{-1}\boldsymbol{\kappa}\right]\frac{\boldsymbol{\kappa}}{\|\boldsymbol{\kappa}\|}-\boldsymbol{x}_{/\!/} \tag{59}$$

where $\boldsymbol{\kappa}=\boldsymbol{\Lambda}\boldsymbol{u}(\vartheta^\star)$ with

$$\vartheta^\star=\frac{1}{2}\arctan\frac{\mathrm{tr}\left\{\boldsymbol{P}_2\boldsymbol{J}(\boldsymbol{x})^{-1}\right\}}{\mathrm{tr}\left\{\boldsymbol{P}_1\boldsymbol{J}(\boldsymbol{x})^{-1}\right\}}. \tag{60}$$

Proof: See Appendix D-B. □

As shown in the proof, the intermediate expression for $L_{/\!/}$ is given by

$$L_{/\!/}=\min_{\vartheta}\ \boldsymbol{u}(\vartheta)^{\mathrm{T}}[\boldsymbol{\Lambda}^{\mathrm{T}}\boldsymbol{J}(\boldsymbol{x})^{-1}\boldsymbol{\Lambda}]\boldsymbol{u}(\vartheta) \tag{61}$$

where $\boldsymbol{\Lambda}=[\boldsymbol{\xi}\quad\boldsymbol{\eta}]/\|\boldsymbol{\xi}\|$. Note that the parallel error is related to the component $\mathbf{x}_{/\!/}^{+}$ in $\mathcal{P}$, which only has two dimensions of freedom and is the column space of $\boldsymbol{\Lambda}$. By the formula of parameter transformation for the Cramér-Rao bound (CRB) [44, Chapter 2.4, Property 5], the term $\boldsymbol{\Lambda}^{\mathrm{T}}\boldsymbol{J}(\boldsymbol{x})^{-1}\boldsymbol{\Lambda}$ is the CRB for $\mathbf{x}_{/\!/}^{+}$. The optimization problem in (61) finds the direction on which the component of $\mathbf{x}_{/\!/}^{+}$ has the minimum variance, and the other dimension of freedom corresponding to the rotation is eliminated.[11]

[10]This can be proved by expressing the deterministic part $\boldsymbol{x}_{/\!/}+\boldsymbol{c}_{/\!/}(\boldsymbol{r})$ and the random part $\mathbf{w}_{/\!/}$ under the orthogonal basis $\{\boldsymbol{\xi},\boldsymbol{\eta}\}$, and it can be shown that the two coordinates of $\mathbf{w}_{/\!/}$ are i.i.d. Gaussian variables.

[11]Note that the direction of the vector $\boldsymbol{\kappa}$ is the same with the eigenvector of second largest eigenvalue of matrix $\boldsymbol{\Xi}\boldsymbol{J}(\boldsymbol{x})^{-1}\boldsymbol{\Xi}$.

3) Bounds of the MFEB: Based on Proposition 7 and 8, the lower and upper bounds for the MFEB are given in the following theorem.

Theorem 1: For arbitrary control policies, the MFEB F is bounded by

$$\underline{F}\leq F\leq\overline{F} \tag{62}$$

with $\underline{F}=F_{\perp}$ given in (53), and

$$\begin{aligned}\overline{F}&=\mathrm{tr}\left\{\left(\boldsymbol{I}-\boldsymbol{D}-\frac{\boldsymbol{\Xi}}{2}\right)\boldsymbol{J}(\boldsymbol{x})^{-1}\right\}-\frac{1}{2}\left\|\begin{bmatrix}\mathrm{tr}\left\{\boldsymbol{P}_1\boldsymbol{J}(\boldsymbol{x})^{-1}\right\}\\\mathrm{tr}\left\{\boldsymbol{P}_2\boldsymbol{J}(\boldsymbol{x})^{-1}\right\}\end{bmatrix}\right\|\\&\quad+(2N-2)\sigma^2.\end{aligned} \tag{63}$$

where $\boldsymbol{P}_1$ and $\boldsymbol{P}_2$ are defined in Proposition 8. The upper bound can be achieved under the control policy

$$\begin{aligned}\boldsymbol{c}^{\star}(\boldsymbol{r})&=\left[\|\boldsymbol{\xi}\|+\nabla\ln p(\boldsymbol{r};\boldsymbol{x})^{\mathrm{T}}\boldsymbol{J}(\boldsymbol{x})^{-1}\boldsymbol{\kappa}\right]\frac{\boldsymbol{\kappa}}{\|\boldsymbol{\kappa}\|}\\&\quad-(\boldsymbol{I}-\boldsymbol{D}-\boldsymbol{\Xi})\boldsymbol{J}(\boldsymbol{x})^{-1}\nabla\ln p(\boldsymbol{r};\boldsymbol{x})-\boldsymbol{x}.\end{aligned} \tag{64}$$

Proof: Combining $F=F_{\perp}+F_{/\!/}$, (57) and the results of Proposition 7 and 8 directly leads to (62). □

C. Discussions and Special Cases

Both the lower bound (53) and the upper bound (63) for the MFEB contain two parts. The first part exhibits the effect of the localization error, where MAF is affected by the quality of the measurements in the form of $\boldsymbol{J}(\boldsymbol{x})^{-1}$. The second part indicates the effect of the control error, which is in the form of $(2N-\epsilon)\sigma^2$. Compared with the total control error for a network of N free agents, i.e. $2N\sigma^2$, there are $\epsilon\in[2,4]$ dimensions subtracted. The main reason is due to the invariance of the formation error to the translation and rotation operators, which removes $\epsilon_0=3$ dimensions of freedom.

Due to the convoluted coupling between network localization and formation control, the exact localization-induced MFEB grows with $\boldsymbol{J}(\boldsymbol{x})^{-1}$ at a rate between the corresponding parts in the upper bound and the lower bound, and the exact control-induced MFEB can only be constrained in the interval $[2N-4,2N-2]\sigma^2$. However, when either the control error or the localization error is absent, the effect resulted from the coupling of the two procedures vanishes. Therefore, in these two special cases, the exact MFEB, rather than its bounds, can be exactly derived.

Case A (Accurate Control): The system is free of the control error and only affected by the localization error. The MFE is obtained by setting $\mathbf{w}_{\perp}=\mathbf{w}_{/\!/}=\mathbf{0}$ when applying (45), i.e.

$$\bar{\ell}=\mathbb{E}_{\mathbf{r}}\{\|\boldsymbol{x}_{\perp}+\boldsymbol{c}_{\perp}(\mathbf{r})\|^2+(\|\boldsymbol{x}_{/\!/}+\boldsymbol{c}_{/\!/}(\mathbf{r})\|-\|\boldsymbol{\xi}\|)^2\}. \tag{65}$$

To derive the bound for the first term, we apply Proposition 7 and set $\sigma=0$ in (53), and this bound is achieved with the control policy (54). On the other hand, Proposition 8 directly gives the bound for the second term in (58) and the corresponding control policy (59). To sum up, the MFEB in this case is given by

$$F_{\mathrm{AC}}=\mathrm{tr}\left\{\left(\boldsymbol{I}-\boldsymbol{D}-\frac{\boldsymbol{\Xi}}{2}\right)\boldsymbol{J}(\boldsymbol{x})^{-1}\right\}-\frac{1}{2}\left\|\begin{bmatrix}\mathrm{tr}\left\{\boldsymbol{P}_1\boldsymbol{J}(\boldsymbol{x})^{-1}\right\}\\\mathrm{tr}\left\{\boldsymbol{P}_2\boldsymbol{J}(\boldsymbol{x})^{-1}\right\}\end{bmatrix}\right\| \tag{66}$$

which can be achieved by the control policy (64).

Case B (Accurate Localization)[12]*:* The actual formation is known in this case, and the MFEB can be derived by designing the optimal control policy according to the geometrical insight of the formation error provided in Fig. 4 and Proposition 5. The orthogonal control vector can be designed as $\boldsymbol{c}_\perp = -\boldsymbol{x}_\perp$, which leads to an expected orthogonal error of $(2N-4)\sigma^2$; and the expected parallel error is given by

$$\bar{\ell}_{/\!/}(\nu) = \nu^2 - \sqrt{2\pi}\sigma\|\boldsymbol{\xi}\|\,\mathrm{Lag}_{1/2}\left(\frac{-\nu^2}{2\sigma^2}\right) + \|\boldsymbol{\xi}\|^2 + 2\sigma^2 \quad (67)$$

where $\nu = \|\boldsymbol{x}_{/\!/} + \boldsymbol{c}_{/\!/}\|$ and $\mathrm{Lag}_{1/2}(\cdot)$ denotes the Laguerre function of order $1/2$. It can be verified that $\bar{\ell}_{/\!/}(\nu)$ is convex w.r.t. ν^2, and thus there exists a unique optimal solution $\nu^\star$ that minimizes the above expression, given by

$$\nu^\star = \max\left\{\left[-2\sigma^2\,g\Big(-\frac{2\sigma}{\sqrt{2\pi}\|\boldsymbol{\xi}\|}\Big)\right]^{1/2},\,0\right\} \quad (68)$$

where g is the inverse of the first-order derivative of $\mathrm{Lag}_{1/2}(\cdot)$. Thus, the MFEB is given by

$$F_{\mathrm{AL}} = \bar{\ell}_{/\!/}(\nu^\star) + (2N-4)\sigma^2 \quad (69)$$

with the function $\bar{\ell}_{/\!/}(\nu)$ defined in (67). The MFEB can be achieved under the control policy[13]

$$\boldsymbol{c}^\star = \frac{\nu^\star}{\|\boldsymbol{\xi}\|}\begin{bmatrix}\boldsymbol{\xi} & \boldsymbol{\eta}\end{bmatrix}\boldsymbol{u}(\vartheta) - \boldsymbol{x}, \quad \forall\vartheta\in[0,2\pi]. \quad (70)$$

Remark 3: For the extended definitions of the formation error given in Section III-C, their bounds are provided as follows. As proved in Section III-C1, the MFE for scalable formations only contains the orthogonal error (37), and thus the MFEB is given by $F_{\mathrm{s}} = F_\perp$. For three-dimensional formations, the expression of the MFEB (62) still holds, but to replace $\boldsymbol{\xi}$ by $\boldsymbol{Z}\boldsymbol{\xi}$ and $\boldsymbol{\eta}$ by $\boldsymbol{Z}^2\boldsymbol{\xi}$ in the corresponding definitions of the matrices $\boldsymbol{\Xi}$, $\boldsymbol{P}_1$ and $\boldsymbol{P}_2$.

V. Integrated Localization and Control

In this section, we develop the ILC algorithm for MAF as shown in Algorithm 1, based on the analytical results derived in the previous section. A sensing strategy and control policy is designed for high-accuracy MAF under limited spectrum resource. Again, we clarify that to implement the developed algorithm in practice, we employ the estimated formation $\hat{\mathbf{x}}$ as a substitute for the actual formation $\boldsymbol{x}$, such as in the related FIMs in (73) and (74) as well as the control vectors by (64), (70) and (77).

A. Sensing Strategy

As observed from (53) and (63), both the upper bound and lower bound of the MFEB are closely related to the FIM. The FIM reflects the quality of the measurements, which is determined by the spectrum resource allocation schemes. Inspired by this relationship and the constraint on the spectrum resource, we introduce $\boldsymbol{w}$ as the *allocation vector* that collects w_{ij} for all links, which denotes the amount of spectrum resource allocated to link (i,j); and W_0 as the total spectrum resource.[14] Besides, we employ the notation $\boldsymbol{J}(\boldsymbol{x};\boldsymbol{w})$ to emphasize that the FIM (4) is a function of the allocation vector $\boldsymbol{w}$. More explicitly,

$$\boldsymbol{J}(\boldsymbol{x};\boldsymbol{w}) = \boldsymbol{J}_{\mathrm{A}} + \sum_{(i,j)\in\mathcal{E}} w_{ij}\boldsymbol{J}_{ij}(\boldsymbol{x}) \quad (71)$$

where $\boldsymbol{J}_{\mathrm{A}}$ is the information provided by the existing measurements (5), which is fixed for the current time slot; and $\boldsymbol{J}_{ij}(\boldsymbol{x})$ is given by (80).

By optimizing the sensing strategy $\boldsymbol{w}$, the MFEB can be reduced. Here, we adopt the upper bound $\overline{F}$ given by (63) as a relaxation of the exact MFEB, and formulate the optimization problem w.r.t. the sensing strategy as minimizing $\overline{F}$ while satisfying the constraint on spectrum resource, i.e.

$$\begin{aligned}\mathscr{P}_0:\quad &\underset{\boldsymbol{w}\in\mathbb{R}_+^{|\mathcal{E}|}}{\text{minimize}}\quad \overline{F}\big(\boldsymbol{J}(\boldsymbol{x};\boldsymbol{w})^{-1}\big)\\ &\text{subject to}\quad \|\boldsymbol{w}\|_1 = W_0.\end{aligned} \quad (72)$$

Due to the non-linear relationship between the upper bound $\overline{F}$ and $\boldsymbol{J}(\boldsymbol{x};\boldsymbol{w})^{-1}$, the above optimization problem (72) is difficult to solve. Hence, we approximate the objective function $\overline{F}(\boldsymbol{J}(\boldsymbol{x};\boldsymbol{w})^{-1})$ by its first-order Taylor expansion at $\boldsymbol{J}(\boldsymbol{x};\boldsymbol{w})^{-1} = \boldsymbol{J}_{\mathrm{A}}^{-1}$, given by

$$\begin{aligned}&\overline{F}^{(1)}\big(\boldsymbol{J}(\boldsymbol{x};\boldsymbol{w})^{-1}\big)\\ &\approx \overline{F}(\boldsymbol{J}_{\mathrm{A}}^{-1}) + \nabla\overline{F}(\boldsymbol{J}_{\mathrm{A}}^{-1})\big(\boldsymbol{J}(\boldsymbol{x};\boldsymbol{w})^{-1} - \boldsymbol{J}_{\mathrm{A}}^{-1}\big)\\ &= \mathrm{tr}\left\{(\boldsymbol{I} - \boldsymbol{D} - \boldsymbol{\Xi}/2 + \boldsymbol{H})\boldsymbol{J}(\boldsymbol{x};\boldsymbol{w})^{-1}\right\} + C\end{aligned} \quad (73)$$

where C denotes the terms unrelated to $\boldsymbol{w}$, and

$$\boldsymbol{H} = -\frac{\mathrm{tr}\left\{\boldsymbol{P}_1\boldsymbol{J}_{\mathrm{A}}^{-1}\right\}\boldsymbol{P}_1 + \mathrm{tr}\left\{\boldsymbol{P}_2\boldsymbol{J}_{\mathrm{A}}^{-1}\right\}\boldsymbol{P}_2}{2\sqrt{\mathrm{tr}\left\{\boldsymbol{P}_1\boldsymbol{J}_{\mathrm{A}}^{-1}\right\}^2 + \mathrm{tr}\left\{\boldsymbol{P}_2\boldsymbol{J}_{\mathrm{A}}^{-1}\right\}^2}}. \quad (74)$$

Mathematically, the first-order Taylor approximation is valid when $\overline{F}$ is close to a linear function, and $\boldsymbol{J}(\boldsymbol{x};\boldsymbol{w})^{-1}$ does not deviate too much from $\boldsymbol{J}_{\mathrm{A}}^{-1}$. Note that although $\overline{F}$ is not strictly linear, it is on a linear order w.r.t. $\boldsymbol{J}(\boldsymbol{x};\boldsymbol{w})^{-1}$, and thus it is reasonable to adopt a linear model for approximation.[15]

Algorithm 1 ILC Algorithm for MAF

```
1: for t = 1 : T do
2:    Allocate the spectrum resource according to (75) and
      obtain the measurements r ;
3:    Estimate the formation using Bayesian filtering;
4:    Determine the control vector c by (64) or (70);
5:    for i = 1 : N do
6:       Each agent controls itself to the target position;
7:    end for
8:    Calculate the FIM J_A for the next time slot.
9: end for
```

[12] The derivation for the conclusions in this case was reported in [40]. Details are omitted here due to space limitation.

[13] The MFEB can be achieved as long as $\mathbf{x}_{/\!/}^{+}$ lies in the circle of radius $\nu^\star$ in the hyperplane $\mathcal{P}$.

[14] When the allocation vector $\boldsymbol{w}$ is specified, we can determine the partition of the band $\{\mathcal{S}_{ij}:(i,j)\in\mathcal{E}\}$ by applying (82) reversely, and then use (81) to design the transmission signals for each ranging link. See Appendix A.

[15] If the conditions do not hold, one can employ the lower bound for the MFEB (53) as the objective function in $\mathscr{P}_0$ (although not as tight as the upper bound to approximate the MFEB), which is strictly linear w.r.t. $\boldsymbol{J}(\boldsymbol{x};\boldsymbol{w})^{-1}$.

In the sense of minimizing the approximate upper bound of MFEB, the optimal strategy for spectrum allocation is the solution to

$$\mathscr{P}_1: \quad \underset{\boldsymbol{w}\in\mathbb{R}_+^m}{\text{minimize}} \quad \overline{F}^{(1)}\big(\boldsymbol{J}(\boldsymbol{x};\boldsymbol{w})^{-1}\big) \qquad \text{subject to} \quad \|\boldsymbol{w}\|_1 = W_0 \tag{75}$$

The above strategy is called the *formation-based allocation* for abbreviation in this paper.

Proposition 9: The optimization problem for formation-based allocation strategy is convex w.r.t. the vector $\boldsymbol{w}$.

Proof: See Appendix E. □

B. Control Policy

We next design two control policies, namely the loosely- and the tightly-integrated formation control.

- The *loosely-integrated control* regards the estimated formation provided by network localization as the actual formation, and designs the control vector based on the estimated formation, as discussed in Section IV-B3 *Case B*. The control vector is given by (70);
- The *tightly-integrated control* adopts the form of the control policy (64), which can achieve the approximated upper bound of the MFEB in theory. This control policy incorporates the statistical information of the measurements in the designed control vector.

In dynamic scenarios, to determine the tightly-integrated control, the term $\varphi_t = p(\boldsymbol{r}^{(1:t)};\boldsymbol{x}^{(t)})$ need to be calculated over time, where $\boldsymbol{r}^{(1:t)}$ denotes all the observations from time slot 1 to t, and $\boldsymbol{x}^{(t)}$ denotes the current formation. This can be obtained in a recursive form

$$\varphi_t = p(\boldsymbol{r}^{(t)};\boldsymbol{x}^{(t)})\int p(\boldsymbol{x}^{(t-1)};\boldsymbol{x}^{(t)})\varphi_{t-1}\mathrm{d}\boldsymbol{x}^{(t-1)}. \tag{76}$$

Note that when deciding the control vector via (64), a key step is to derive the term $\nabla \ln p(\boldsymbol{r};\boldsymbol{x})$. With the above expression for $p(\boldsymbol{r}^{(1:t)};\boldsymbol{x}^{(t)})$, this term can be calculated as

$$\nabla \ln \varphi_t = \frac{\int \nabla p(\boldsymbol{x}^{(t-1)};\boldsymbol{x}^{(t)})\varphi_{t-1}\mathrm{d}\boldsymbol{x}^{(t-1)}}{\int p(\boldsymbol{x}^{(t-1)};\boldsymbol{x}^{(t)})\varphi_{t-1}\mathrm{d}\boldsymbol{x}^{(t-1)}} + \nabla \ln p(\boldsymbol{r}^{(t)};\boldsymbol{x}^{(t)}) \tag{77}$$

where $p(\boldsymbol{x}^{(t-1)};\boldsymbol{x}^{(t)})$ is obtained from the movement model (7), and $\nabla \ln p(\boldsymbol{r}^{(t)};\boldsymbol{x}^{(t)})$ is derived by the measurement model (3). The integrals can be calculated numerically by methods such as Monte-Carlo integration.

Remark 4: Since the information related to the position and orientation of the formation is absent in the discussed scenario, the absolute localization error bound $\boldsymbol{J}(\boldsymbol{x})^{-1}$ may diverge over time, and so is the recursive expression (76). To overcome this difficulty, we incorporate extra regularization constraints to eliminate the three dimensions accounting for translation and rotation. In the beginning of time slot $t+1$, we update $\varphi_t(\boldsymbol{x}) = \varphi_t(\boldsymbol{x}_1,\cdots,\boldsymbol{x}_n)$ by:

- Calculate $\boldsymbol{m}_i = \int \boldsymbol{x}_i\varphi_t(\boldsymbol{x})\mathrm{d}\boldsymbol{x}$ for agent $i=1$ and 2;
- Update the function by $\varphi_t(\boldsymbol{z}) \leftarrow \varphi_t(\boldsymbol{x})$ where $\boldsymbol{z} = \boldsymbol{G}(\vartheta_t)(\boldsymbol{x} - \boldsymbol{1}_N \otimes \boldsymbol{m}_1)$ with $\boldsymbol{u}(-\vartheta_t)^{\mathrm{T}}(\boldsymbol{m}_2 - \boldsymbol{m}_1) = 0$.

The purpose of the above operations is to construct a dynamic *filtering frame*, in which the "center" of agent 1 locates at the origin, and the "center" of agent 2 on the y-axis. The accumulated rotation $\vartheta^{(t)} = \sum_{\tau=1}^{t}\vartheta_\tau$ of the filtering frame in the global frame is recorded, in order to transform the control vector $\boldsymbol{c}_{\mathrm{f}}$ calculated in this frame back to the global frame $\boldsymbol{c}_{\mathrm{g}} = \boldsymbol{G}(-\vartheta^{(t)})\boldsymbol{c}_{\mathrm{f}}$. This approach can prevent the error bound as well as (76) from diverging. A more rigorous analysis of the above procedure is left for future work.

VI. Numerical Results

Consider a two-dimensional formation of N agents, and we assume that any pair of agents can make measurements with each other. The total spectrum resource of the system is set as $W_0 = N/3$. For the measurement signal with spectrum resource w, the variance of the ranging noise is ς^2/w m^2, where ς^2 is the ranging variance per resource unit. Recall that the variance of the control error is denoted by σ^2.

This section is divided into two aspects. Part A and B validate the performance gains of the proposed algorithms in a single time slot, where the network includes three agents and the target formation is a uniform line with the inter-agent distance of 10 m; part C and D further study the performance of the ILC scheme in dynamic scenarios, and the effects of more general formation geometries and system parameters.

A. Control Policy

First, we compare the MFEs that can be achieved by different control policies, when measurements of various accuracy are provided. The proposed loosely- and the tightly-integrated control policies are compared with a *potential-based* approach [32], where agent i determines its target position by minimizing the potential function

$$V_i(\boldsymbol{x}) = \sum_{j\neq i}\left(\|\boldsymbol{x} - \hat{\mathbf{x}}_j\| - \|\boldsymbol{\xi}_i - \boldsymbol{\xi}_j\|\right)^2 \tag{78}$$

in which $\hat{\mathbf{x}}_j$ is the estimated position of agent j. Three agents are considered, and the total spectrum resource $W_0 = N/3 = 1$ is uniformly allocated to all the 3 ranging links, i.e. $w_{ij} = W_0/3 = 1/3$ for $\forall\ (i,j) \in \mathcal{E}$. Therefore, when the ranging variance is ς^2 m^2, the variance for each measurement link is $\varsigma_{ij}^2 = 3\varsigma^2$ m^2; and with different values of ς^2, measurements of different accuracies can be obtained. The agents estimate their positions by the maximum likelihood criteria.

As shown in Fig. 5, the proposed methods can achieve a significant performance gain over the potential-based method. Note that when there exists control error (the dashed batch), the performance curves are nearly parallel to the corresponding curves when there is no control error, and thus the gaps among control policies are almost the same. Then we compare the proposed control policies when there is no control error, and the tightly-integrated control outperforms the loosely-integrated control by about 45% in terms of the MFE.

B. Sensing Strategy

Next we compare the spectrum resource consumption by different allocation strategies to achieve a given MFE. We

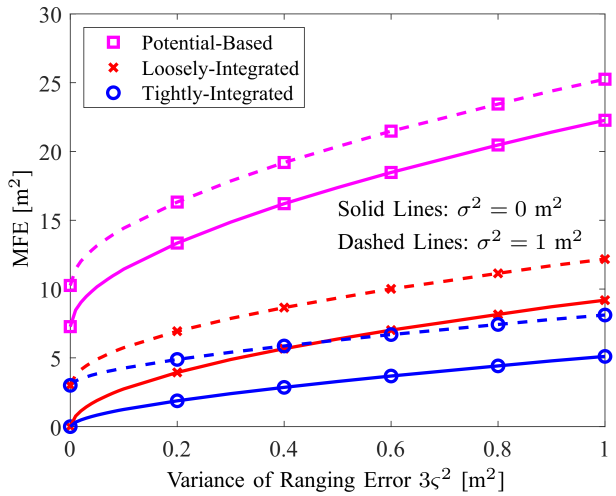

Fig. 5. The MFEs as a function of the ranging variance ς^2 by the potential-based, the loosely- and the tightly-integrated control. The solid lines are obtained when the system is free of control error, and the dashed lines are obtained when the variance of the control error $\sigma^2 = 1$ m^2.

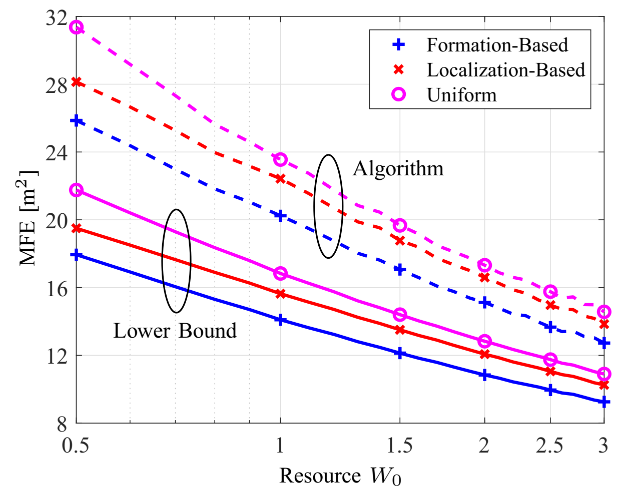

Fig. 6. The MFEs and the lower bounds as a function of total resource by the formation-based allocation, the localization-based and the uniform allocation.

consider a rectangular area of 40×20 m^2, and the 3 agents are uniformly distributed within the area. Suppose the agents are provided with the existing measurements $\mathbf{r}^- = \boldsymbol{x} + \mathbf{n}$ with $\mathbf{n} \sim \mathcal{N}(\mathbf{0}, 25\boldsymbol{I})$ m, where $\boldsymbol{x}$ is the true formation. The ranging variance is set as $\varsigma^2 = 1$ m^2. The formation-based allocation strategy proposed in Section V-A is compared with another two strategies:

- The *localization-based allocation* which aims to minimize $\mathrm{tr}\left\{\boldsymbol{J}(\boldsymbol{x};\boldsymbol{w})^{-1}\right\}$ under the same constraints [22];
- The *uniform allocation* which divides the spectrum equally for all possible links.

The goal of the first strategy is to minimize the lower bound of network localization error. By comparing with it, we exhibit the gain to optimize resource allocation directly toward the MAF, rather than the localization procedure. The second strategy serves as a baseline algorithm: it is simple and the implementation does not require extra computational effort. Besides, for the succeeding two procedures (estimation and control), we employ the maximum likelihood criteria and the proposed tightly-integrated control policy, respectively.

The relationship between the MFE and the amount of the resource W_0 is presented in Fig. 6. We make the following observations. First, for certain accuracy of the formation, a large portion of spectrum resource can be saved when applying the proposed sensing strategy instead of the other two strategies. Take the MFE $\bar{\ell} = 16$ m^2 as an example. For practical algorithms, the required spectrum resources are respectively 1.73, 2.17 and 2.47 for the three allocation strategies, and hence the proposed allocation strategy can save 20% of spectrum resource than the localization-based allocation, and 30% than the uniform allocation; while for theoretical lower bound, the needed spectrum resource are 0.70, 0.92 and 1.15, and the proposed strategy outperforms the other two methods by 25% and 40%, respectively.[16] Second, the theoretical bound of the proposed method is lower than the other two methods. Note that the proposed strategy only aims at minimizing the upper bound of the MFEB; however, this advantage also holds for the lower bound in most scenarios. Third, the MFE achieved by the applied algorithm is about 50% higher than its theoretical lower bound when the available resource is $W_0 = 1$.

[16] Note that the percentage of the spectrum resource reduction does not vary much for different value of the MFE.

C. Integrated Design

Next we evaluate the performance gain of the proposed ILC scheme in dynamic scenarios. We consider target formations of different agent number N, with the ith agent locating at $10 \times [i, \mathrm{mod}(i,2)]^{\mathrm{T}}$ m. The system is observed for T time slots, which is long enough for the MFE to reach a stable state. In the experiment, we take $T = 150$ and use the last 50 time slots to calculate the time-averaged MFE. The proposed scheme is compared with another two schemes:

- The *separate design* employs the localization-based allocation strategy in network localization and the loosely-integrated policy in formation control;
- The *baseline* employs the uniform allocation strategy and the potential-based control policy.

The first scheme is proposed to represent the optimal performance that can be achieved by separately optimizing each individual procedure: 1) the resource is allocated merely to optimize the localization; 2) the control vector is optimal assuming that the formation estimate is accurate. The gain of integrated design can be exhibited by comparing the proposed scheme with the first scheme. The second scheme also follows a separate-design manner, which adopts the basic approaches in literature and thus can serve as a baseline. In addition, we suppose that in the estimation phase, the result is generated from an unbiased Gaussian distribution with the CRB as the covariance matrix; and we set $\sigma^2 = \varsigma^2 = 1$ m^2.

Fig. 7 depicts the time-averaged MFE by the three schemes. We make the following observations. First, a separate optimization for the two procedures can reduce the MFE by

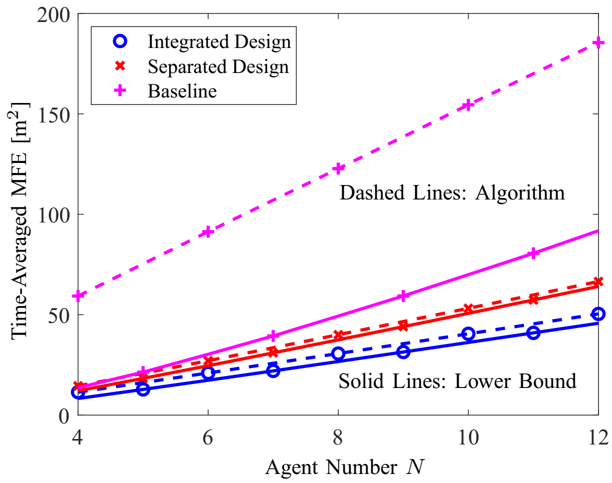

Fig. 7. The time-averaged MFEs and the corresponding lower bounds as a function of the agent number by the integrated design, the separated design and the baseline scheme.

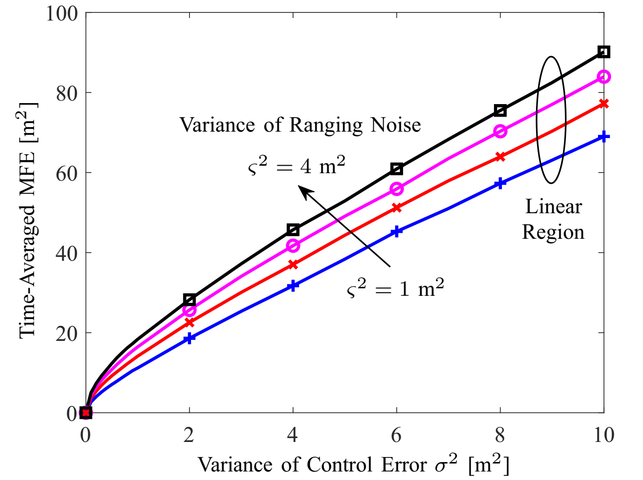

Fig. 8. The time-averaged MFE as a function of the control error by the ILC algorithm under different ranging noise variances.

about 70%, although the lower bound does not reduce by such a large portion. This result validates the importance of strategy design in achieving accurate formation under resource constraints. Second, the MFE can be further reduced by 30% via the integrated design over network localization and formation control, which validates that a more rational resource allocation and information utilization can improve the accuracy of formation. Finally, the time-averaged MFE of the ILC scheme grows almost linearly with the agent number. In other words, as the number of agents increases, the MFE per agent stays constant for this scheme.[17] It implies that the distortion between the the actual formation and the target formation is invariant with the formation size.[18] Therefore, we conclude that the integrated scheme is promising to deal with the MAF task for large formations, and it shows superior performance than the other two schemes.

D. System Parameters

Finally, we demonstrate the effects of the variance of the control error σ^2 and the ranging noise ς^2 on the performance of the proposed ILC algorithm. We consider a network of 4 agents, with the target formation as a 10 m $\times$ 10 m square; other settings are the same as the previous section.

As can be observed from Fig. 8, the time-averaged MFE grows with both parameters in a complicated way, due to the coupling between network localization and formation control. However, we can employ its theoretical bounds to explain the phenomenon in a special case, where the variance of the control error is much larger than that of the ranging noise. In this scenario, the historical information vanishes due to the large control error over adjacent time slots, and thus the CRB is approximately linear with the variance of the ranging noise and free of the control error. Then according to Section IV, the localization-part error is proportional to the CRB, and thus the variance of the ranging noise; and the control-part error is proportional to the variance of the control error. This leads to linear growths of the MFE with respect to both parameters in the regions as we marked in Fig. 8.

[17] Recall that the formation error is the sum of the squared distances that all the agents move. Hence the MFE per agent characterizes how far each agent deviates from their target positions, which intuitively represents the distortion of the actual formation from the target formation.

[18] In network localization, with the same configuration for the total spectrum resource as is used here, the network localization error (NLE) per agent is constant (Section "boundedness of error evolution" in [23]). While the definitions of the MFE and NLE are closely related, Fig. 7 also suggests the MFE per agent is constant. The rigorous analysis for the linear growth of the MFE with the agent number is left for future work.

VII. Conclusion

In this paper, we established a theoretical framework for high-accuracy MAF via integrated localization and control. First, we proposed a new performance metric called the formation error to quantify the difference between two formations, and then we obtained a closed-form expression, revealed some properties, and presented a geometrical interpretation for the metric. Second, we derived the theoretical bounds for the MFE for arbitrary control policies, and developed an ILC algorithm by joint optimization over the network localization and the formation control procedure. Finally, simulation results showed that the proposed ILC algorithm can significantly improve the accuracy of the MAF, and presented the formation performance under various network parameters.

Appendix A
FIM for Network Localization

Recall that all the ranging links are collected in set $\mathcal{E}$, and the measurements in vector $\mathbf{d}$. The received waveform $\mathsf{r}_{ij}(t)$ for a ranging link between agent i and j is modeled as $\mathsf{r}_{ij}(t) = s_{ij}(t-\text{delay})+\text{noise}$, where $s_{ij}(t)$ is the transmission waveform. Then the FIM for the entire formation is given by

$$\boldsymbol{J}_{\mathbf{d}}(\boldsymbol{x}) = \sum_{(i,j)\in\mathcal{E}} \left(\int_{-\infty}^{\infty} f^2 |S_{ij}(f)| \mathrm{d}f \right) \boldsymbol{J}_{ij} \tag{79}$$

where $S_{ij}(f)$ denotes the Fourier transform of $s_{ij}(t)$, and

$$\boldsymbol{J}_{ij} = \frac{1}{\varsigma_{ij}^2} \left[(\boldsymbol{e}_i - \boldsymbol{e}_j) \otimes \boldsymbol{u}(\phi_{ij}) \right] \left[(\boldsymbol{e}_i - \boldsymbol{e}_j) \otimes \boldsymbol{u}(\phi_{ij}) \right]^{\mathrm{T}} \tag{80}$$

with $\boldsymbol{e}_i$ an $N \times 1$ vectors with all 0's but 1 in the ith element, and ϕ_{ij} the direction between agent i and j.

Given an aggregated signal $S(f)$ for the entire formation system, which spans over the band $\mathcal{S}_0$, an allocation of the spectrum resource is to divide $\mathcal{S}_0$ into $|\mathcal{E}|$ non-overlapping sub-bands $\{\mathcal{S}_{ij} : (i,j) \in \mathcal{E}\}$, and design the transmission signal on link (i,j) as

$$S_{ij}(f) = \begin{cases} S(f) & f \in \mathcal{S}_{ij} \\ 0 & f \in \mathcal{S}_0 \setminus \mathcal{S}_{ij} \end{cases}. \tag{81}$$

In this manner, there is no interference between the ranging signals. The spectrum resource of link (i,j) is defined as

$$w_{ij} = \int_{-\infty}^{\infty} f^2 |S_{ij}(f)| \mathrm{d}f = \int_{\mathcal{S}_{ij}} f^2 |S(f)| \mathrm{d}f \tag{82}$$

and the total spectrum resource as $W_0 = \int_{\mathcal{S}_0} f^2 |S(f)| \mathrm{d}f$.

Appendix B
Proof of Proposition 1

We address the problem (19) by minimizing the squared formation distance first over $\boldsymbol{t}$ and then over $\boldsymbol{s}$. Denote the result of the first step by $\varphi(\boldsymbol{s})$, which is given by

$$\varphi(\boldsymbol{s}) = \min_{\boldsymbol{k},\vartheta} \Big\{ \sum_{i=1}^{N} \big\| \boldsymbol{s}_i - \big[\boldsymbol{G}_2(\vartheta)(\boldsymbol{q}_i - \bar{\boldsymbol{q}}) + \widetilde{\boldsymbol{k}} \big] \big\|^2 \Big\} \tag{83}$$

where $\boldsymbol{s}_i$ and $\boldsymbol{q}_i$ are the position of agent i in formation $\boldsymbol{s}$ and $\boldsymbol{q}$, respectively, and $\bar{\boldsymbol{q}} \in \mathbb{R}^2$ is the center of the formation $\boldsymbol{q}$. Set the derivatives of $\varphi(\boldsymbol{s})$ w.r.t. $\widetilde{\boldsymbol{k}}$ and ϑ be zero, and we can obtain

$$\{\widetilde{\boldsymbol{k}}^\star, \vartheta^\star\} = \Big\{ \bar{s}, \arctan \frac{\widetilde{\boldsymbol{q}}_\perp^{\mathrm{T}} \widetilde{\boldsymbol{s}}}{\widetilde{\boldsymbol{q}}^{\mathrm{T}} \widetilde{\boldsymbol{s}}} \Big\}. \tag{84}$$

Substituting (84) into (83) leads to

$$\begin{aligned} \varphi(\boldsymbol{s}) &= \|\widetilde{\boldsymbol{s}}\|^2 + \|\widetilde{\boldsymbol{q}}\|^2 - 2\widetilde{\boldsymbol{s}}^{\mathrm{T}} (\widetilde{\boldsymbol{q}} \cos\vartheta^\star + \widetilde{\boldsymbol{q}}_\perp \sin\vartheta^\star) \\ &= \|\widetilde{\boldsymbol{s}}\|^2 + \|\widetilde{\boldsymbol{q}}\|^2 - 2\|\widetilde{\boldsymbol{q}}\| \sqrt{\widetilde{\boldsymbol{s}}^{\mathrm{T}} \boldsymbol{Q} \widetilde{\boldsymbol{s}}}. \end{aligned} \tag{85}$$

Then we minimize the above function over $\boldsymbol{s} \in \mathcal{F}(\boldsymbol{p})$, which indicates that $\widetilde{\boldsymbol{s}} = \boldsymbol{G}(\vartheta)\widetilde{\boldsymbol{p}}$ for some $\vartheta \in [0, 2\pi)$. Substitute the form into the expression, and it can be shown that

$$\varphi(\boldsymbol{s}) = \|\widetilde{\boldsymbol{p}}\|^2 + \|\widetilde{\boldsymbol{q}}\|^2 - 2\|\widetilde{\boldsymbol{q}}\| \sqrt{\widetilde{\boldsymbol{p}}^{\mathrm{T}} \boldsymbol{Q} \widetilde{\boldsymbol{p}}} \tag{86}$$

is a constant function for any $\boldsymbol{s}$. Thus, $d(\boldsymbol{p}, \boldsymbol{q}) = \sqrt{\min_{\boldsymbol{s}} \varphi(\boldsymbol{s})}$ is equivalent to (20).

Appendix C
Proof of Proposition 3

We first present another form for the formation distance. It can be shown that the inequality

$$\frac{\sqrt{(\boldsymbol{p}^{\mathrm{T}}\boldsymbol{q})^2 + (\boldsymbol{p}^{\mathrm{T}}\boldsymbol{R}\boldsymbol{q})^2}}{\|\boldsymbol{p}\|\|\boldsymbol{q}\|} \le 1 \tag{87}$$

holds, and thus the left-hand side can be defined as $\cos\theta_{\boldsymbol{p},\boldsymbol{q}}$. Then the formation distance (20) can be rewritten as

$$d(\boldsymbol{p}, \boldsymbol{q}) = \sqrt{\|\boldsymbol{p}\|^2 + \|\boldsymbol{q}\|^2 - 2\|\boldsymbol{p}\|\|\boldsymbol{q}\| \cos\theta_{\boldsymbol{p},\boldsymbol{q}}}. \tag{88}$$

This form is consistent with *the law of cosines*.

First, we prove the identity of indiscernibles for the defined function, i.e. $d(\mathcal{F}(\boldsymbol{p}), \mathcal{F}(\boldsymbol{q})) = 0$ when $\mathcal{F}(\boldsymbol{p}) = \mathcal{F}(\boldsymbol{q})$. Since the equation holds only when $\cos\theta_{\boldsymbol{p},\boldsymbol{q}} = 1$, which indicates that $\boldsymbol{p} \in \mathrm{span}\{\boldsymbol{q}, \boldsymbol{R}\boldsymbol{q}\} \in \mathcal{F}(\boldsymbol{q})$, and thus $\mathcal{F}(\boldsymbol{p}) = \mathcal{F}(\boldsymbol{q})$.

Then, we prove that the function is symmetry, i.e. $d(\boldsymbol{p}, \boldsymbol{q}) = d(\boldsymbol{q}, \boldsymbol{p})$. Note that $\boldsymbol{R} = -\boldsymbol{R}^{\mathrm{T}}$, and it follows that

$$\sqrt{(\boldsymbol{p}^{\mathrm{T}}\boldsymbol{q})^2 + (\boldsymbol{p}^{\mathrm{T}}\boldsymbol{R}\boldsymbol{q})^2} = \sqrt{(\boldsymbol{q}^{\mathrm{T}}\boldsymbol{p})^2 + (\boldsymbol{q}^{\mathrm{T}}\boldsymbol{R}\boldsymbol{p})^2}. \tag{89}$$

The above equation directly leads to $d(\boldsymbol{p}, \boldsymbol{q}) = d(\boldsymbol{q}, \boldsymbol{p})$.

Last, we show that the triangular inequality holds for the defined function, i.e.

$$d(\boldsymbol{p}, \boldsymbol{q}) + d(\boldsymbol{q}, \boldsymbol{s}) \ge d(\boldsymbol{p}, \boldsymbol{s}). \tag{90}$$

According to (88) and its geometrical interpretation, a sufficient condition for the above inequality is

$$\theta_{\boldsymbol{p},\boldsymbol{q}} + \theta_{\boldsymbol{q},\boldsymbol{s}} \ge \theta_{\boldsymbol{p},\boldsymbol{s}} \tag{91}$$

since a tetrahedron can be constructed under this case. Assume w.l.o.g. that the norms of all the formations equal to 1, and they center at origin. To prove (91), we define the left-hand side of the inequality as a function, and aim to find its minima, i.e.

$$\min_{\boldsymbol{q}} \; h(\boldsymbol{q}) = \sum_{\boldsymbol{\gamma} \in \{\boldsymbol{p}, \boldsymbol{s}\}} \arccos \sqrt{(\boldsymbol{q}^{\mathrm{T}}\boldsymbol{\gamma})^2 + (\boldsymbol{q}^{\mathrm{T}}\boldsymbol{R}\boldsymbol{\gamma})^2} \tag{92}$$

subject to $\boldsymbol{q}^{\mathrm{T}}\boldsymbol{d}_x = \boldsymbol{q}^{\mathrm{T}}\boldsymbol{d}_y = 0$, and $\|\boldsymbol{q}\|^2 = 1$. The Lagrange function for the constrained optimization problem writes

$$\mathcal{L}(\boldsymbol{q}) = h(\boldsymbol{q}) + \lambda_1 \boldsymbol{q}^{\mathrm{T}}\boldsymbol{d}_x + \lambda_2 \boldsymbol{q}^{\mathrm{T}}\boldsymbol{d}_y + \lambda_3(\boldsymbol{q}^{\mathrm{T}}\boldsymbol{q} - 1). \tag{93}$$

Set the derivative w.r.t. $\boldsymbol{q}$ be $\mathbf{0}$, and we obtain

$$\begin{aligned} &- \sum_{\boldsymbol{\gamma} \in \{\boldsymbol{p}, \boldsymbol{s}\}} \frac{(\boldsymbol{q}^{\mathrm{T}}\boldsymbol{\gamma})\boldsymbol{\gamma} + (\boldsymbol{q}^{\mathrm{T}}\boldsymbol{R}\boldsymbol{\gamma})\boldsymbol{R}\boldsymbol{\gamma}}{\sqrt{1 - (\boldsymbol{q}^{\mathrm{T}}\boldsymbol{\gamma})^2 - (\boldsymbol{q}^{\mathrm{T}}\boldsymbol{R}\boldsymbol{\gamma})^2}\sqrt{(\boldsymbol{q}^{\mathrm{T}}\boldsymbol{\gamma})^2 + (\boldsymbol{q}^{\mathrm{T}}\boldsymbol{R}\boldsymbol{\gamma})^2}} \\ &+ \lambda_1 \boldsymbol{d}_x + \lambda_2 \boldsymbol{d}_y + 2\lambda_3 \boldsymbol{q} = \mathbf{0} \end{aligned} \tag{94}$$

which implies $\lambda_1 = \lambda_2 = 0$. Thus, the optimal solution $\boldsymbol{q}^\star$ can be expressed in the following form

$$\boldsymbol{q}^\star = \rho_1 \begin{bmatrix} \boldsymbol{p} & \boldsymbol{R}\boldsymbol{p} \end{bmatrix} \boldsymbol{u}(\phi_1) + \rho_2 \begin{bmatrix} \boldsymbol{s} & \boldsymbol{R}\boldsymbol{s} \end{bmatrix} \boldsymbol{u}(\phi_2) \tag{95}$$

and the parameters ρ_1, ρ_2, ϕ_1 and ϕ_2 are to be determined. Use $\|\boldsymbol{q}^\star\| = 1$, and that the ratios between the coefficients of $\boldsymbol{p}$ and $\boldsymbol{R}\boldsymbol{p}$ in (94) and (95) are equal, and it follows that

$$\rho_1^2 + \rho_2^2 + 2\rho_1\rho_2 \cos\theta_{\boldsymbol{p},\boldsymbol{s}} = 1. \tag{96}$$

By (95) and (96), we can prove that

$$\cos h(\boldsymbol{q}^\star) = \cos\theta_{\boldsymbol{p},\boldsymbol{s}}. \tag{97}$$

Since $\cos(\cdot)$ decreases monotonously in $[0, \pi]$, the above conclusion is equivalent to $\theta_{\boldsymbol{p},\boldsymbol{q}} + \theta_{\boldsymbol{q},\boldsymbol{s}} \ge \theta_{\boldsymbol{p},\boldsymbol{s}}$.

Appendix D
Proof of Proposition 7 and 8

We use the variational method over control policies to derive the expected orthogonal and parallel error bounds. Note that the expectation is taken over the random measurements $\mathbf{r}$.

A. Mean Orthogonal Error

The solution is divided into two steps. First, certain assumptions are made to define a subset of control policies, and the optimal control policy is designed for each case; then we compare the performance of the optimal control policies and choose the best among them. The condition is set as

$$\int (\boldsymbol{x}_\perp + \boldsymbol{c}_\perp(\boldsymbol{r}))p(\boldsymbol{r};\boldsymbol{x})\mathrm{d}\boldsymbol{r} = \boldsymbol{s} \tag{98}$$

and thus the control policy $\boldsymbol{c}_\perp$ satisfies

$$\int \boldsymbol{c}_\perp(\boldsymbol{r})p(\boldsymbol{r};\boldsymbol{x})\mathrm{d}\boldsymbol{r} = \boldsymbol{s} - \boldsymbol{x}_\perp. \tag{99}$$

Note that $\boldsymbol{c}_\perp(\boldsymbol{r})$ is independent with the actual formation $\boldsymbol{x}$, then taking derivative w.r.t. $\boldsymbol{x}^{\mathrm{T}}$ of both sides gives

$$\int \boldsymbol{c}_\perp(\boldsymbol{r})\nabla \ln p(\boldsymbol{r};\boldsymbol{x})^{\mathrm{T}} p(\boldsymbol{r};\boldsymbol{x})\mathrm{d}\boldsymbol{r} = -(\boldsymbol{I} - \boldsymbol{D} - \boldsymbol{\Xi}). \tag{100}$$

Then we find the optimal solution in the set of the control policies which satisfy the constraints (99) and (100), that is denoted by $\mathcal{C}(\boldsymbol{s})$. Suppose $\boldsymbol{c}_\perp^+(\boldsymbol{r}) = \boldsymbol{c}_\perp(\boldsymbol{r}) + \lambda \boldsymbol{g}(\boldsymbol{r}) \in \mathcal{C}(\boldsymbol{s})$ with $\boldsymbol{c}_\perp(\boldsymbol{r}) \in \mathcal{C}(\boldsymbol{s})$, then the increment $\lambda \boldsymbol{g}(\boldsymbol{r})$ satisfies

$$\int \boldsymbol{g}(\boldsymbol{r})p(\boldsymbol{r};\boldsymbol{x})\mathrm{d}\boldsymbol{r} = \boldsymbol{0} \tag{101}$$

$$\int \boldsymbol{g}(\boldsymbol{r})\nabla \ln p(\boldsymbol{r};\boldsymbol{x})^{\mathrm{T}} p(\boldsymbol{r};\boldsymbol{x})\mathrm{d}\boldsymbol{r} = \boldsymbol{O}. \tag{102}$$

According to (46), the expected orthogonal error under control policy $\boldsymbol{c}_\perp^+(\boldsymbol{r})$ is given by (omit $(2N-4)\sigma^2$)

$$\bar{\ell}_\perp(\lambda) = \int \|\boldsymbol{x}_\perp + \boldsymbol{c}_\perp(\boldsymbol{r}) + \lambda \boldsymbol{g}(\boldsymbol{r})\|^2 p(\boldsymbol{r};\boldsymbol{x})\mathrm{d}\boldsymbol{r} \tag{103}$$

To design the optimal control policy, set the derivative of $\bar{\ell}_\perp$ w.r.t. λ as 0 when $\lambda = 0$, and we obtain

$$2\int \boldsymbol{g}(\boldsymbol{r})^{\mathrm{T}}(\boldsymbol{x}_\perp + \boldsymbol{c}_\perp^\star(\boldsymbol{r};\boldsymbol{s}))p(\boldsymbol{r};\boldsymbol{x})\mathrm{d}\boldsymbol{r} = 0. \tag{104}$$

where $\boldsymbol{c}_\perp^\star(\boldsymbol{r};\boldsymbol{s})$ is the optimal control in the set $\mathcal{C}(\boldsymbol{s})$. Note that the function $\boldsymbol{g}$ can be arbitrarily chosen, it follows that

$$\boldsymbol{x}_\perp + \boldsymbol{c}_\perp^\star(\boldsymbol{r};\boldsymbol{s}) = \boldsymbol{m} + \boldsymbol{M}\nabla \ln p(\boldsymbol{r};\boldsymbol{x}) \tag{105}$$

where $\boldsymbol{m} \in \mathbb{R}^{2N}$ and $\boldsymbol{M} \in \mathbb{R}^{2N\times 2N}$. Substitute the above form into (99) and (100), and we can determine the parameters. Then the optimal control policy $\boldsymbol{c}_\perp^\star(\boldsymbol{r};\boldsymbol{s})$ is given by[19]

$$(\boldsymbol{s} - \boldsymbol{x}_\perp) - (\boldsymbol{I} - \boldsymbol{D} - \boldsymbol{\Xi})\boldsymbol{J}(\boldsymbol{x})^{-1}\nabla \ln p(\boldsymbol{r};\boldsymbol{x}) \tag{106}$$

and the corresponding minimum expected orthogonal error is

$$L_\perp(\boldsymbol{s}) = \|\boldsymbol{s}\|^2 + \mathrm{tr}\left\{(\boldsymbol{I} - \boldsymbol{D} - \boldsymbol{\Xi})\boldsymbol{J}(\boldsymbol{x})^{-1}\right\}. \tag{107}$$

When changing the value of $\boldsymbol{s}$, all the control policies can be covered. By the form of the achievable lower bound, we can assert that when $\boldsymbol{s} = \boldsymbol{0}$, the optimal expected orthogonal error can be achieved, which is given by

$$L_\perp = \mathrm{tr}\left\{(\boldsymbol{I} - \boldsymbol{D} - \boldsymbol{\Xi})\boldsymbol{J}(\boldsymbol{x})^{-1}\right\} \tag{108}$$

when applying the control policy

$$\boldsymbol{c}_\perp^\star(\boldsymbol{r}) = -(\boldsymbol{I} - \boldsymbol{D} - \boldsymbol{\Xi})\boldsymbol{J}(\boldsymbol{x})^{-1}\nabla \ln p(\boldsymbol{r};\boldsymbol{x}) - \boldsymbol{x}_\perp. \tag{109}$$

[19] If the FIM $\boldsymbol{J}(\boldsymbol{x})$ is not invertible, the pseudoinverse $\boldsymbol{J}(\boldsymbol{x})^\dagger$ will replace the inverse $\boldsymbol{J}(\boldsymbol{x})^{-1}$ in all the succeeding equations. This convention also holds for the derivation in the parallel subspace.

B. Mean Parallel Error

Follow the same procedure in Appendix D-A, and suppose the condition is given by

$$\int \|\boldsymbol{x}_{/\!/} + \boldsymbol{c}_{/\!/}(\boldsymbol{r})\| p(\boldsymbol{r};\boldsymbol{x})\mathrm{d}\boldsymbol{r} = \varrho \tag{110}$$

and the other constraint on the derivative is

$$\int \left\{\boldsymbol{\Xi}\boldsymbol{\phi} + \|\boldsymbol{x}_{/\!/} + \boldsymbol{c}_{/\!/}(\boldsymbol{r})\|\nabla \ln p(\boldsymbol{r};\boldsymbol{x})\right\}p(\boldsymbol{r};\boldsymbol{x})\mathrm{d}\boldsymbol{r} = \boldsymbol{0}. \tag{111}$$

Given the control policies $\boldsymbol{c}_{/\!/}(\boldsymbol{r})$ and $\boldsymbol{c}_{/\!/}^+(\boldsymbol{r}) = \boldsymbol{c}_{/\!/}(\boldsymbol{r}) + \lambda \boldsymbol{g}(\boldsymbol{r})$, which both meet the above conditions. Then by taking derivatives of the constraints w.r.t. $\boldsymbol{c}_{/\!/}(\boldsymbol{r})$, function $\boldsymbol{g}(\boldsymbol{r})$ satisfies

$$\int \boldsymbol{g}(\boldsymbol{r})^{\mathrm{T}}\boldsymbol{\phi} p(\boldsymbol{r};\boldsymbol{x})\mathrm{d}\boldsymbol{r} = 0 \tag{112}$$

$$\int \boldsymbol{g}(\boldsymbol{r})^{\mathrm{T}}\left[\boldsymbol{\Phi}\boldsymbol{\Xi} + \boldsymbol{\phi}\nabla \ln p(\boldsymbol{r};\boldsymbol{x})^{\mathrm{T}}\right] p(\boldsymbol{r};\boldsymbol{x})\mathrm{d}\boldsymbol{r} = \boldsymbol{0}^{\mathrm{T}}. \tag{113}$$

where

$$\boldsymbol{\phi} = \frac{\boldsymbol{x}_{/\!/} + \boldsymbol{c}_{/\!/}(\boldsymbol{r})}{\|\boldsymbol{x}_{/\!/} + \boldsymbol{c}_{/\!/}(\boldsymbol{r})\|}, \quad \boldsymbol{\Phi} = \frac{\boldsymbol{I} - \boldsymbol{\phi}\boldsymbol{\phi}^{\mathrm{T}}}{\|\boldsymbol{x}_{/\!/} + \boldsymbol{c}_{/\!/}(\boldsymbol{r})\|}. \tag{114}$$

Set the derivative of the mean parallel error

$$\bar{\ell}_{/\!/}(\lambda) = \int (\|\boldsymbol{x}_{/\!/} + \boldsymbol{c}_{/\!/}(\boldsymbol{r}) + \lambda \boldsymbol{g}(\boldsymbol{r})\| - \|\boldsymbol{\xi}\|)^2 p(\boldsymbol{r};\boldsymbol{x})\mathrm{d}\boldsymbol{r} \tag{115}$$

w.r.t. λ be zero when $\lambda = 0$, i.e.

$$2\int \boldsymbol{g}(\boldsymbol{r})^{\mathrm{T}}[\boldsymbol{x}_{/\!/} + \boldsymbol{c}_{/\!/}(\boldsymbol{r}) - \|\boldsymbol{\xi}\|\boldsymbol{\phi}]p(\boldsymbol{r};\boldsymbol{x})\mathrm{d}\boldsymbol{r} = 0 \tag{116}$$

which indicates that

$$\boldsymbol{x}_{/\!/} + \boldsymbol{c}_{/\!/}(\boldsymbol{r}) = \lambda_0\boldsymbol{\phi} + \left[\boldsymbol{\Phi}\boldsymbol{\Xi} + \boldsymbol{\phi}\nabla \ln p(\boldsymbol{r};\boldsymbol{x})^{\mathrm{T}}\right]\boldsymbol{\lambda} \tag{117}$$

for some $\lambda_0 \in \mathbb{R}$ and $\boldsymbol{\lambda} \in \mathbb{R}^2$. Note that $\boldsymbol{\Phi}\boldsymbol{\phi} = \boldsymbol{0}$, and then we 1) multiply $\boldsymbol{\phi}^{\mathrm{T}}$ on the left of both sides, which leads to

$$\|\boldsymbol{x}_{/\!/} + \boldsymbol{c}_{/\!/}(\boldsymbol{r})\| = \lambda_0 + \nabla \ln p(\boldsymbol{r};\boldsymbol{x})^{\mathrm{T}}\boldsymbol{\lambda} \tag{118}$$

and 2) multiply $\boldsymbol{\Phi}$ on the left of both sides, which leads to

$$\frac{(\boldsymbol{\Xi}\boldsymbol{\lambda}) - [\boldsymbol{\phi}^{\mathrm{T}}(\boldsymbol{\Xi}\boldsymbol{\lambda})]\boldsymbol{\phi}}{\|\boldsymbol{x}_{/\!/} + \boldsymbol{c}_{/\!/}(\boldsymbol{r})\|^2} = \boldsymbol{0}. \tag{119}$$

Substituting (118) into (110) leads to $\lambda_0 = \varrho$; then according to (119), $\boldsymbol{\phi} =$ is a constant unit vector in $\mathcal{P}$ and thus can be expressed as $\boldsymbol{\phi} = -\boldsymbol{\Lambda}\boldsymbol{u}(\vartheta)$. Then, (111) gives that

$$\boldsymbol{\lambda}(\vartheta) = \boldsymbol{J}(\boldsymbol{x})^{-1}\boldsymbol{\Lambda}\boldsymbol{u}(\vartheta). \tag{120}$$

where any value of $\vartheta \in [0, 2\pi)$ maps to a corresponding saddle point. The expected parallel error is given by

$$L_{/\!/}(\varrho, \vartheta) = (\varrho - \|\boldsymbol{\xi}\|)^2 + \boldsymbol{u}(\vartheta)^{\mathrm{T}}\boldsymbol{\Lambda}^{\mathrm{T}}\boldsymbol{J}(\boldsymbol{x})^{-1}\boldsymbol{\Lambda}\boldsymbol{u}(\vartheta). \tag{121}$$

It can be observed that the first term is minimized when $\varrho = \|\boldsymbol{\xi}\|$, and the second term can be expressed as

$$\frac{1}{2}\Big(\mathrm{tr}\left\{\boldsymbol{\Xi}\boldsymbol{J}(\boldsymbol{x})^{-1}\right\} + \boldsymbol{\psi}\big(\boldsymbol{J}(\boldsymbol{x})\big)^{\mathrm{T}}\boldsymbol{u}(2\vartheta)\Big) \tag{122}$$

where $\boldsymbol{\psi}\big(\boldsymbol{J}(\boldsymbol{x})\big)^{\mathrm{T}} \triangleq [\mathrm{tr}\left\{\boldsymbol{P}_1\boldsymbol{J}(\boldsymbol{x})^{-1}\right\}\ \mathrm{tr}\left\{\boldsymbol{P}_2\boldsymbol{J}(\boldsymbol{x})^{-1}\right\}]$. Then according to Cauchy-Schwarz inequality, the solution $\vartheta^\star$ that minimizes the above expression is given by (60). Then the optimal expected parallel error is given by

$$L_{/\!/} = \frac{1}{2}\left(\mathrm{tr}\left\{\boldsymbol{\Xi}\boldsymbol{J}(\boldsymbol{x})^{-1}\right\} - \|\boldsymbol{\psi}(\boldsymbol{J}(\boldsymbol{x}))\|\right). \tag{123}$$

To derive the control policy, by (117) we have

$$\|\boldsymbol{x}_{/\!/} + \boldsymbol{c}_{/\!/}\| = \|\boldsymbol{\xi}\| + \nabla \ln p(\boldsymbol{r};\boldsymbol{x})^{\mathrm{T}}\boldsymbol{\lambda}^{\star} \tag{124}$$

and note that

$$\frac{\boldsymbol{x}_{/\!/} + \boldsymbol{c}_{/\!/}}{\|\boldsymbol{x}_{/\!/} + \boldsymbol{c}_{/\!/}\|} = \boldsymbol{\phi} = -\boldsymbol{J}(\boldsymbol{x})\boldsymbol{\lambda}^{\star} \tag{125}$$

where $\boldsymbol{\lambda}^{\star} = \boldsymbol{\lambda}(\vartheta^{\star})$ can be obtained by substituting (60) into (120). The above two expressions directly lead to (59).

Appendix E
Proof of Proposition 9

The conclusion can be drawn by two steps. First, we claim that the matrix $\boldsymbol{I} - \boldsymbol{D} - \boldsymbol{\Xi}/2 + \boldsymbol{H}$ is positive semidefinite. It is sufficient to show that both $\boldsymbol{I} - \boldsymbol{D} - \boldsymbol{\Xi}$ and $\boldsymbol{A} = \boldsymbol{\Xi}/2 + \boldsymbol{H}$ are positive semidefinite. The first term is positive semidefinite since $\mathcal{D} \oplus \mathcal{P}$ is a subspace of the entire space. For the second term, note that

$$\boldsymbol{H} = [\sin\vartheta \cdot \boldsymbol{P}_1 + \cos\vartheta \cdot \boldsymbol{P}_2]/2 \tag{126}$$

for some ϑ. Take any vector $\boldsymbol{s} \in \mathbb{R}^{2N}$, which can be expressed as $\boldsymbol{s} = \beta_1\boldsymbol{\xi} + \beta_2\boldsymbol{\eta} + \boldsymbol{b}$ with $\boldsymbol{\xi}^{\mathrm{T}}\boldsymbol{b} = \boldsymbol{\eta}^{\mathrm{T}}\boldsymbol{b} = 0$, and we can have the following inequality

$$\begin{aligned}\frac{\boldsymbol{s}^{\mathrm{T}}\boldsymbol{A}\boldsymbol{s}}{\|\boldsymbol{\xi}\|^4} &= \beta_1^2 + \beta_2^2 + 2\beta_1\beta_2\sin\vartheta + (\beta_1^2 - \beta_2^2)\cos\vartheta \\ &\geq \beta_1^2 + \beta_2^2 - \sqrt{(2\beta_1\beta_2)^2 + (\beta_1^2 - \beta_2^2)^2} = 0\end{aligned} \tag{127}$$

which implies $\boldsymbol{A} \succeq 0$.

Second, we show that for any weight matrix $\boldsymbol{W} \succeq 0$,

$$\begin{aligned}\mathscr{P}: \quad &\underset{\boldsymbol{w}\in\mathbb{R}_{+}^{m}}{\text{minimize}} \quad \mathrm{tr}\left\{\boldsymbol{W}\boldsymbol{J}(\boldsymbol{x};\boldsymbol{w})^{-1}\right\} \\ &\text{subject to} \quad \|\boldsymbol{w}\|_1 = W_0\end{aligned} \tag{128}$$

is a convex optimization problem w.r.t. $\boldsymbol{w}$. Since the constraint is affine (convex), we need to show that the objective function $f(\boldsymbol{w})$ is convex w.r.t. $\boldsymbol{w}$, which is equivalent to proving that $g(s) = f(\boldsymbol{w} + s\boldsymbol{\varepsilon})$ is convex w.r.t. $s \in \mathbb{R}_{+}$ for $\forall \boldsymbol{w}, \boldsymbol{\varepsilon} \in \mathbb{R}_{+}^{m}$. This condition can be verified after some algebra [45], and the details are omitted due to the space limitation.

References

[1] N. Kantas, S. S. Singh, and A. Doucet, "Distributed maximum likelihood for simultaneous self-localization and tracking in sensor networks," *IEEE Trans. Signal Process.*, vol. 60, no. 10, pp. 5038–5047, Jun. 2012.

[2] N. H. Motlagh, M. Bagaa, and T. Taleb, "UAV-based IoT platform: A crowd surveillance use case," *IEEE Commun. Mag.*, vol. 55, no. 2, pp. 128–134, Feb. 2017.

[3] L. Paull, G. Huang, M. Seto, and J. J. Leonard, "Communication-constrained multi-AUV cooperative SLAM," in *Proc. IEEE Int. Conf. on Robotics and Automation*, Seattle, WA, USA, May 2008, pp. 509–516.

[4] J. Cheng, J. Cheng, M. Zhou, F. Liu, S. Gao, and C. Liu, "Routing in Internet of vehicles: A review," *IEEE Trans. Intell. Transp. Syst.*, vol. 16, no. 5, pp. 2339–2352, Oct. 2015.

[5] Y. Zeng, R. Zhang, and T. J. Lim, "Wireless communications with unmanned aerial vehicles: Opportunities and challenges," *IEEE Commun. Mag.*, vol. 54, no. 5, pp. 36–42, May 2016.

[6] P. Tokekar, J. V. Hook, D. Mulla, and V. Isler, "Sensor planning for a symbiotic UAV and UGV system for precision agriculture," *IEEE Trans. Robot.*, vol. 32, no. 6, pp. 1498–1511, Dec. 2016.

[7] Y. Cao, W. Yu, W. Ren, and G. Chen, "An overview of recent progress in the study of distributed multi-agent coordination," *IEEE Trans. Ind. Informat.*, vol. 9, no. 1, pp. 427–438, Feb. 2013.

[8] K.-K. Oh and H.-S. Ahn, "Formation control and network Localization via orientation alignment," *IEEE Trans. Autom. Control*, vol. 59, no. 2, pp. 540–545, Feb. 2014.

[9] S. Gezici, Z. Tian, G. B. Giannakis, H. Kobayashi, A. F. Molisch, H. V. Poor, and Z. Sahinoglu, "Localization via ultra-wideband radios: A look at positioning aspects for future sensor networks," *IEEE Signal Process. Mag.*, vol. 22, no. 4, pp. 70–84, Jul. 2005.

[10] M. Z. Win, F. Meyer, Z. Liu, W. Dai, S. Bartoletti, and A. Conti, "Efficient multisensor localization for the Internet of Things," *IEEE Signal Process. Mag.*, vol. 35, no. 5, pp. 153–167, Sep. 2018.

[11] K. Witrisal, P. Meissner, E. Leitinger, Y. Shen, C. Gustafson, F. Tufvesson, K. Haneda, D. Dardari, A. F. Molisch, A. Conti, and M. Z. Win, "High-accuracy localization for assisted living: 5G systems will turn multipath channels from foe to friend," *IEEE Signal Process. Mag.*, vol. 33, no. 2, pp. 59–70, Mar. 2016.

[12] M. Z. Win, A. Conti, S. Mazuelas, Y. Shen, W. M. Gifford, D. Dardari, and M. Chiani, "Network localization and navigation via cooperation," *IEEE Commun. Mag.*, vol. 49, no. 5, pp. 56–62, May 2011.

[13] M. Z. Win, Y. Shen, and W. Dai, "A theoretical foundation of network localization and navigation," *Proc. IEEE*, vol. 106, no. 7, pp. 1136–1165, Jul. 2018.

[14] S. Mazuelas, Y. Shen, and M. Z. Win, "Spatiotemporal Information Coupling in Network Navigation," *IEEE Trans. Inf. Theory*, vol. 64, no. 12, pp. 7759–7779, Dec. 2018.

[15] Y. Shen, H. Wymeersch, and M. Z. Win, "Fundamental limits of wideband localization – Part II: Cooperative networks," *IEEE Trans. Inf. Theory*, vol. 56, no. 10, pp. 4981–5000, Oct. 2010.

[16] Y. Shang, W. Ruml, Y. Zhang, and M. P. J. Fromherz, "Localization from mere connectivity," in *Proc. ACM Int. Symp. Mobile Ad Hoc Netw. & Comput.*, Annapolis, MD, USA, Jun. 2003, pp. 201–212.

[17] P. Biswas, T.-C. Lian, T.-C. Wang, and Y. Ye, "Semidefinite programming based algorithms for sensor network localization," *ACM Trans. Sensor Networks*, vol. 2, no. 2, pp. 188–220, May 2006.

[18] Z. Lin, T. Han, R. Zheng, and M. Fu, "Distributed localization for 2-D sensor networks with bearing-only measurements under switching topologies," *IEEE Trans. Signal Process.*, vol. 64, no. 23, pp. 6345–6359, Dec. 2016.

[19] Z. Lin, M. Fu, and Y. Diao, "Distributed self-localization for relative position sensing networks in 2D space," *IEEE Trans. Signal Process.*, vol. 63, no. 14, pp. 3751–3761, Jul. 2015.

[20] Y. Diao, Z. Lin, and M. Fu, "A barycentric coordinate based distributed localization algorithm for sensor networks," *IEEE Trans. Signal Process.*, vol. 62, no. 18, pp. 4760–4771, Sep. 2014.

[21] M. Z. Win, W. Dai, Y. Shen, G. Chrisikos, and H. V. Poor, "Network operation strategies for efficient localization and navigation," *Proc. IEEE*, vol. 106, no. 7, pp. 1224–1254, Jul. 2018.

[22] W. Dai, Y. Shen, and M. Z. Win, "A computational geometry framework for efficient network localization," *IEEE Trans. Inf. Theory*, vol. 64, no. 2, pp. 1317–1339, Feb. 2018.

[23] T. Wang, Y. Shen, A. Conti, and M. Z. Win, "Network navigation with scheduling: Error evolution," *IEEE Trans. Inf. Theory*, vol. 63, no. 11, pp. 7509–7534, Nov. 2017.

[24] J. N. Ash and R. L. Moses, "On the relative and absolute positioning errors in self-localization systems," *IEEE Trans. Signal Process.*, vol. 56, no. 11, pp. 5668 – 5679, Jun. 2008.

[25] Q. Shi, S. Kyperountas, N. S. Correal, and F. Niu, "Performance analysis of relative location estimation for multihop wireless sensor networks," *IEEE J. Sel. Areas Commun.*, vol. 23, no. 4, pp. 830–838, Apr. 2005.

[26] N. Patwari, A. O. Hero, M. Perkins, N. S. Correal, and R. J. O'Dea, "Relative location estimation in wireless sensor networks," *IEEE Trans. Signal Process.*, vol. 51, no. 8, pp. 2137 – 2148, Aug. 2003.

[27] M. Ye, B. D. O. Anderson, and C. Yu, "Bearing-only measurement self-localization, velocity consensus and formation control," *IEEE Trans. Aerosp. Electron. Syst.*, vol. 53, no. 2, pp. 575–586, Apr. 2017.

[28] W. Ren, R. W. Beard, and E. M. Atkins, "Information consensus in multivehicle cooperative control," *IEEE Control Syst. Mag.*, vol. 27, no. 2, pp. 71–82, Apr. 2007.

[29] T. Balch and R. C. Arkin, "Behavior-based formation control for multirobot teams," *IEEE Trans. Robot. Autom.*, vol. 14, no. 6, pp. 926–939, Dec. 1998.

[30] M. Deghat, B. D. O. Anderson, and Z. Lin, "Combined flocking and distance-based shape control of multi-agent formations," *IEEE Trans. Autom. Control*, vol. 61, no. 7, pp. 1824–1837, Jul. 2016.

[31] K. K. Oh, M. C. Park, and H. S. Ahn, "A survey of multi-agent formation control," *Automatica.*, vol. 53, no. s, pp. 424–440, Mar. 2015.

[32] M. Cao, C. Yu, and B. D. Anderson, "Formation control using range-only measurements," *Automatica.*, vol. 47, no. 4, pp. 776–781, Apr. 2011.

[33] J. A. Fax and R. M. Murray, "Information Flow and Cooperative Control of Vehicle Formations," *IEEE Trans. Autom. Control*, vol. 49, no. 9, pp. 1465–1476, Sep. 2004.

[34] Z. Lin, B. Francis, and M. Maggiore, "Necessary and sufficient graphical conditions for formation control of unicycles," *IEEE Trans. Autom. Control*, vol. 50, no. 1, pp. 121–127, Jan. 2005.

[35] Z. Lin, L. Wang, Z. Han, and M. Fu, "Distributed formation control of multi-agent systems using complex Laplacian," *IEEE Trans. Autom. Control*, vol. 59, no. 7, pp. 1765–1777, Jul. 2014.

[36] X. Dong, B. Yu, Z. Shi, and Y. Zhong, "Time-varying formation control for unmanned aerial vehicles: Theories and applications," *IEEE Trans. Control Syst. Technol.*, vol. 23, no. 1, pp. 174–188, Jan. 2015.

[37] K.-K. Oh and H.-S. Ahn, "Distributed formation control based on orientation alignment and position estimation," *Int. J. Control, Automation, Syst*, vol. 16, no. 3, pp. 1112–1119, Jun. 2018.

[38] Z. Han, K. Guo, L. Xie, and Z. Lin, "Integrated relative localization & leader-follower formation control," *IEEE Trans. Autom. Control*, vol. 1, no. 99, pp. 1–1, Feb. 2018.

[39] K.-K. Oh and H.-S. Ahn, "Formation control of mobile agents based on distributed position estimation," *IEEE Trans. Autom. Control*, vol. 58, no. 3, pp. 737–742, Mar. 2013.

[40] Y. Cai and Y. Shen, "Integrated localization and control for accurate multi-agent formation," in *Proc. IEEE Int. Conf. Commun.*, Kansas City, USA, May 2018, pp. 1 – 6.

[41] Y. Shen and M. Z. Win, "Fundamental limits of wideband localization – Part I: A general framework," *IEEE Trans. Inf. Theory*, vol. 56, no. 10, pp. 4956–4980, Oct. 2010.

[42] V. G. Rao and D. S. Bernstein, "Naive control of the double integrator," *IEEE Control Syst. Mag.*, vol. 21, no. 5, pp. 86 – 97, Oct. 2001.

[43] S. Mazuelas, A. Conti, J. C. Allen, and M. Z. Win, "Soft range information for network localization," *IEEE Trans. Signal Process.*, vol. 66, no. 12, pp. 3155–3168, Jun. 2018.

[44] H. L. Van Trees, Detection, estimation, and modulation theory, optimum array processing. New Jersey: John Wiley & Sons, 2004.

[45] S. Boyd and L. Vandenberghe, Convex optimization. New York, NY, USA: Cambridge University Press, 2004.